

AD \_\_\_\_\_

GRANT NUMBER DAMD17-94-J-4367

TITLE: Development of an Inverse Technique to Estimate the  
Ultrasound Field During Chest Wall and Breast Hyperthermia

PRINCIPAL INVESTIGATOR: Charles L. Thomas, Ph.D.

CONTRACTING ORGANIZATION: University of Utah  
Salt Lake City, Utah 84112

REPORT DATE: September 1998

TYPE OF REPORT: Final

PREPARED FOR: Commander  
U.S. Army Medical Research and Materiel Command  
Fort Detrick, Frederick, Maryland 21702-5012

DISTRIBUTION STATEMENT: Approved for public release;  
distribution unlimited

The views, opinions and/or findings contained in this report are those of the author(s) and should not be construed as an official Department of the Army position, policy or decision unless so designated by other documentation.

DTIC QUALITY INSPECTED 4

19991208 160

# REPORT DOCUMENTATION PAGE

Form Approved  
OMB No. 0704-0188

Public reporting burden for this collection of information is estimated to average 1 hour per response, including the time for reviewing instructions, searching existing data sources, gathering and maintaining the data needed, and completing and reviewing the collection of information. Send comments regarding this burden estimate or any other aspect of this collection of information, including suggestions for reducing this burden, to Washington Headquarters Services, Directorate for Information Operations and Reports, 1215 Jefferson Davis Highway, Suite 1204, Arlington, VA 22202-4302, and to the Office of Management and Budget, Paperwork Reduction Project (0704-0188), Washington, DC 20503.

1. AGENCY USE ONLY (Leave blank)

2. REPORT DATE  
September 1998

3. REPORT TYPE AND DATES COVERED  
Final (1 Aug 94 - 31 Jul 98)

4. TITLE AND SUBTITLE

Development of an Inverse Technique to Estimate the  
Ultrasound Field During Chest Wall and Breast  
Hyperthermia

5. FUNDING NUMBERS

DAMD17-94-J-4367

6. AUTHOR(S)

Charles L. Thomas, Ph.D.

7. PERFORMING ORGANIZATION NAME(S) AND ADDRESS(ES)

University of Utah  
Salt Lake City, Utah 84112

8. PERFORMING ORGANIZATION  
REPORT NUMBER

9. SPONSORING/MONITORING AGENCY NAME(S) AND ADDRESS(ES)

Commander  
U.S. Army Medical Research and Materiel Command  
Fort Detrick, Frederick, Maryland 21702-5012

10. SPONSORING/MONITORING  
AGENCY REPORT NUMBER

11. SUPPLEMENTARY NOTES

12a. DISTRIBUTION / AVAILABILITY STATEMENT

Approved for public release; distribution unlimited

12b. DISTRIBUTION CODE

13. ABSTRACT (Maximum 200)

The goal of this research was to develop a clinical system for improved numerical modeling of ultrasound propagation through breast tissue and the post-mastectomy chest wall for use in patient treatment planning of hyperthermia cancer treatments. This has included the following: Development of an efficient numerical model that predicts the ultrasound behavior based on nodal tissue parameters. The tissue parameters are set using a combination of accepted literature values and experimental data acquired using a patient geometry and tissue attenuation acquisition system developed as part of this program. The power input to the model is determined using experimental transducer power field data (collected with a hydrophone), a transducer model, and an inverse optimization scheme that significantly reduces the error in the transducer model. Initial plans had included using the inverse technique to optimize the nodal tissue parameters, however, experiments with clinical thermocouple probes showed scatter as large as the error in the ultrasonic tissue attenuation measurements, making the optimization unnecessary.

14. SUBJECT TERMS

Breast Cancer

15. NUMBER OF PAGES

66

16. PRICE CODE

17. SECURITY CLASSIFICATION  
OF REPORT

Unclassified

18. SECURITY CLASSIFICATION  
OF THIS PAGE

Unclassified

19. SECURITY CLASSIFICATION  
OF ABSTRACT

Unclassified

20. LIMITATION OF ABSTRACT

Unlimited

NSN 7540-01-280-5500

Standard Form 298 (Rev. 2-89)  
Prescribed by ANSI Std. Z39-18  
298-102

## FOREWORD

Opinions, interpretations, conclusions and recommendations are those of the author and are not necessarily endorsed by the U.S. Army.

\_\_\_\_ Where copyrighted material is quoted, permission has been obtained to use such material.

\_\_\_\_ Where material from documents designated for limited distribution is quoted, permission has been obtained to use the material.

621 Citations of commercial organizations and trade names in this report do not constitute an official Department of Army endorsement or approval of the products or services of these organizations.

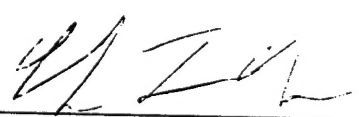
\_\_\_\_ In conducting research using animals, the investigator(s) adhered to the "Guide for the Care and Use of Laboratory Animals," prepared by the Committee on Care and use of Laboratory Animals of the Institute of Laboratory Resources, national Research Council (NIH Publication No. 86-23, Revised 1985).

\_\_\_\_ For the protection of human subjects, the investigator(s) adhered to policies of applicable Federal Law 45 CFR 46.

\_\_\_\_ In conducting research utilizing recombinant DNA technology, the investigator(s) adhered to current guidelines promulgated by the National Institutes of Health.

\_\_\_\_ In the conduct of research utilizing recombinant DNA, the investigator(s) adhered to the NIH Guidelines for Research Involving Recombinant DNA Molecules.

\_\_\_\_ In the conduct of research involving hazardous organisms, the investigator(s) adhered to the CDC-NIH Guide for Biosafety in Microbiological and Biomedical Laboratories.

  
\_\_\_\_  
PI - Signature

12-1-98  
\_\_\_\_  
Date

## Table of Contents

Introduction	1
Program Description and Goals	1
Task Description and Milestones	4
Outline of Accomplishments	5
Summary of Accomplishments:	
Program Summary	7
1 <sup>st</sup> Year Summary	8
2 <sup>nd</sup> Year Summary	8
3 <sup>rd</sup> Year Summary	13
4 <sup>th</sup> Year Accomplishments	
Subsystem 1: Ultrasound Based Anatomy and Attenuation Measurement	26
Three Dimensional Ultrasonic Attenuation Field Measurement	26
Patient Geometry Acquisition and Registration	33
Subsystem 2: Experimental SAR Measurement	44
Subsystem 3: Model Development	52
Subsystem 4: Inverse Technique	53
Concluding Remarks	60
References	61



## Introduction

This document is a final report presenting the results of a four year grant. This introduction includes a brief description of the subject, goals, and scope of the research project, along with a description of the relationship of this work to that of previous researchers. Following this description is a milestone chart showing the focus areas and a timeline of the work accomplished. The introductory section ends with a brief summary of the final program accomplishments followed by a more detailed review of the results of the first three years of the program. The main body of the report is a detailed description of the accomplishments during the final year of the program. This is followed by some concluding remarks addressing the significance of the research accomplishments and anticipated future uses of these results.

## Program Description and Goals

Hyperthermia has been shown to be an efficacious adjuvant therapy in the treatment of recurrent breast cancer.[1,2,3] One of the most flexible and proven methods to induce hyperthermia is ultrasound. In order to optimally utilize such clinical devices it is essential that the operator have the ability to accurately plan a treatment. The clinical hyperthermia situation is diagrammed in Figure 1. A treatment plan consists of a defined motion path and applied transducer power that will raise the temperature of the tumor to a desired set point for a specified time while minimizing the effect on surrounding tissue. The treatment plan must be adjusted for tissue geometry, absorption, and desired temperature history specific to each patient. Planning a treatment begins with the accurate estimation of the absorbed power field created by the ultrasound transducer. Thus, the ability to accurately estimate this field is critical to producing a proper and effective treatment plan.

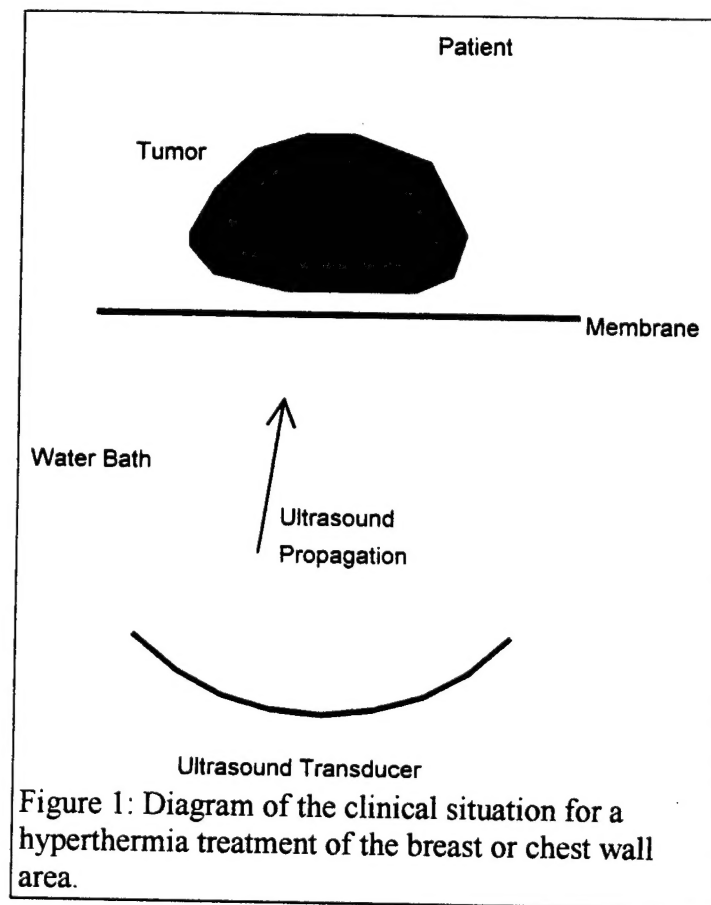


Figure 1: Diagram of the clinical situation for a hyperthermia treatment of the breast or chest wall area.

It is the goal of this research to provide improved numerical modeling of ultrasound propagation through breast tissue and the post-mastectomy chest wall for use in patient treatment planning of hyperthermia cancer treatments. With this improved model the clinician can plan an ultrasound hyperthermia treatment so as to produce the required thermal dose while minimizing patient pain due to excessive temperature or ultrasound-tissue interactions. A clinical system is

being constructed to combine model results with experiments in an inverse technique to estimate the absorbed power field in the breast and chest wall during ultrasound hyperthermia. This improved planning will aid the clinicians in providing better hyperthermia treatments, which will improve treatment response rates.

The system under development consists of the following subsystems:

1. An ultrasonic B-mode imager based clinical data acquisition system used to obtain patient anatomy and measure the attenuation of ultrasound by the body tissue.
2. A clinical technique using an ultrasound treatment system to directly measure absorbed power at specific points.
3. An improved model of ultrasound propagation through breast tissue.
4. An inverse technique that integrates experimental measurements and modeling results to obtain the "best" prediction of the ultrasound power deposition field.

The B-mode diagnostic ultrasound imager in Subsystem 1 is used to construct a geometric model based upon each patient's anatomy and to measure the ultrasound attenuation coefficient at selected areas within the tissue region. In Subsystem 2 the clinical treatment system is used in a scanning protocol to locate thermocouples imbedded in the breast tissue. The response of these thermocouples to the scanned ultrasound gives a direct measure of the power deposition at that point. Subsystem 3 is an ultrasound propagation and power deposition model. For this model we have considered 2 options:

- a) Hybrid Green's Function Model - Ultrasound propagation from the transducer into the breast is modeled with a hybrid of Green's function solutions used in the homogenous water region and a finite element solution of the acoustic wave equation in the inhomogeneous breast region.
- b) Parabolic Model - This is a forward marching parabolic model that is quite fast, but does not take into account reflected energy at interfaces.

Subsystem 4 is an iterative inverse technique that optimizes the parameters of the power deposition model by forcing the model results to match the experimental measurements. The model is used to predict the power deposition at the thermocouple locations, the error between model and experiment is measured, and the error values are used to adjust the model parameters for the next iteration.

This improved power deposition model will be useful in the development of more accurate path planning for hyperthermia treatment. As such it will provide a clinically useful tool that can serve as the base for the development of more accurate treatment path planning, more accurate control techniques, and eventually, higher success rates in hyperthermia treatment with reduced patient discomfort during treatment.

# **Task Description and Milestones:**

Task Description and Milestones:	Quarter															
	1	2	3	4	5	6	7	8	9	10	11	12	13	14	15	16
Finite Element Model	x	x	x	x	x	x	x	x								
Hybrid Green's Function Model					x	x	x	x	x	x						
Parabolic Model					x	x	x	x	x	x	x	x				
Inverse Technique	x	x							x	x	x	x	x	x	x	x
Ultrasonic Hardware Development	x	x	x	x												
Attenuation Measurement 1D			x	x	x	x	x	x								
Attenuation Measurement 3D									x	x	x	x	x	x	x	
Geometry Acquisition/Registration									x	x	x	x	x	x	x	x
<i>in vivo</i> SAR technique	x								x	x	x	x	x	x	x	x
System Integration/Phantom Tests										x	x	x	x	x		
Clinical Data Gathering												x	o	o	o	o

## **Outline of Accomplishments:**

### **1<sup>st</sup> Year Accomplishments:**

#### Subsystem 1: Geometry Acquisition and Attenuation Measurement

- Acquisition of ultrasonic B-scan instrument.
- Development of interface hardware to isolate analog A-line information.
- Acquisition of high speed A/D system and development of control software.
- Investigation of reflection based acoustic attenuation measurement techniques.

#### Subsystem 2: Experimental SAR Measurement

- Initial discussions and verification of equipment.

#### Subsystem 3: Model Development

- Development and testing of a 2D finite element based model.
- Identification of alternative solutions.

#### Subsystem 4: Inverse Technique

- Initial discussions.

### **2<sup>nd</sup> Year Accomplishments:**

#### Subsystem 1: Geometry Acquisition and Attenuation Measurement

- Development of Log Spectral Difference software for measuring the acoustic attenuation from a single A-line.
- Development and testing of a Force/Balance test apparatus for direct measurement of acoustic attenuation.

#### Subsystem 2: Experimental SAR Measurement

- No work accomplished.

#### Subsystem 3: Model Development

- Extension of the 2D FE model to three dimensions. Combination of the FE model with an integral method model to improve the speed of the model.
- Development of a 3D parabolic model as a much faster, possibly less accurate alternative.
- Development of a 3D Green's Function model for use as the "gold standard" with which the other models will be compared.
- Initial model comparisons.

#### Subsystem 4: Inverse Technique

- No progress.

### **3<sup>rd</sup> Year Accomplishments:**

#### Subsystem 1: Geometry Acquisition and Attenuation Measurement

- Laboratory hardware was developed to provide 3D scanning capability for the medical B-scan imager. Clinical hardware is now essentially complete.
- Software to produce a 3D, tissue attenuation map from the A-mode signals was completed and is undergoing verification testing.

- Software and hardware for clinical patient geometry acquisition is approximately 50% complete.

#### Subsystem 2: Experimental SAR Measurement

- Thermocouple based beam plots have been performed to calibrate the ultrasound power field in water for specific transducers.
- Experiments have been conducted in water and are beginning using cast agar phantoms.
- Preliminary in-vivo experiments were conducted on a dog.
- A finite difference model has been constructed to help interpret the experimental measurements.

#### Subsystem 3: Model Development

- The parabolic model has been selected for use in regions of low acoustic contrast. In these regions the model is quite fast and loses little accuracy when compared to the Green's Function Model. The Green's Function Model can be used in high contrast areas (close to ribs, etc.)
- User interface developed allowing specification of the volume modeled, the acoustic power input as a 2D complex pressure function, and model parameters; density, sound velocity, and absorption at each node.

#### Subsystem 4: Inverse Technique

- Basic algorithm development. Optimization runs on simple geometries.

### **4<sup>th</sup> Year Accomplishments:**

#### Subsystem 1: Geometry Acquisition and Attenuation Measurement

- Verification tests for clinical system for 3D attenuation mapping.
- Software and hardware for clinical patient geometry acquisition completed.
- Verification tests completed.

#### Subsystem 2: Experimental SAR Measurement

- Probe orientation effects on the SAR measurements were investigated experimentally.
- A series of new probes were designed, constructed and tested.
- A final design was proposed for future work.

#### Subsystem 3: Model Development

- The model was completed in the 3<sup>rd</sup> year. No work was accomplished on this subsystem during the 4<sup>th</sup> year.

#### Subsystem 4: Inverse Technique

- Subsystem integration completed.
- Technique used successfully to optimize the input power model.
- Given the level of scatter in the experimental SAR measurements, the optimization model was not used to adjust nodal attenuation values.

## Program Summary

The four year research effort has resulted in an improved power deposition model for hyperthermia treatment planning. The model is significantly faster than previous power deposition models used for treatment planning. It is more flexible, accepting tissue geometry and attenuation values measured clinically. It uses an inverse optimization scheme to improve the fit between the model parameters and clinical measurements. This optimization has been implemented for tuning the power input model and can potentially be implemented for tuning tissue property data. Extensive testing has shown that existing thermocouple probes are not well suited to measure SAR. An improved thermocouple has been designed, but construction, testing, and implementation will be left to future researchers. This system is now being integrated into the hyperthermia treatment facility at the University of Utah Hospital.

During the first two years of the research program, a parabolic numerical model was developed that is dramatically faster than finite element models or models based on integral equations. The model is capable of processing a model with  $10^6$  nodes in approximately 2 minutes (using a Sun Sparc 20 workstation). The model handles free space boundary conditions much more conveniently than the finite element model. The model accurately handles the forward propagation of ultrasonic energy, but does not account for reflected energy. This is not a significant limitation since the low acoustic contrast occurring in tissue does not give rise to large reflections. Comparisons to an integral model showed a good match except when bone was present. This is considered acceptable since treatment requiring significant insonation near bones is unlikely due to patient pain. These results are being submitted for journal publication.

The system includes an ultrasonic B-scan based patient geometry acquisition and attenuation measurement system that allows the model nodal parameters to be conveniently adjusted to match the tissue geometry and attenuation of each patient. This system requires a pre-treatment scanning session where an operator acquires the patient geometry, a technician identifies the significant tissue regions, and the attenuation calculations are performed. The system has been shown to identify tissue geometry to an accuracy of  $\pm 1$  mm and attenuation values to within 10%.

An inverse optimization technique was developed to adjust model parameters to minimize the error between model predicted SAR values and experimental measurements. The technique was developed successfully, however, accurate experimental SAR measurements have not been achieved. The model has been used successfully to generate an accurate model for input ultrasound energy. Here the inverse technique was used to adjust the surface velocity profile of a model of the ultrasound transducer to provide an optimal match to measurements made with a hydrophone probe. Experimental results showed that when a transducer model using a piston like velocity profile was replaced with the same model using an optimized profile, the error between experimental hydrophone measurements and the model prediction was reduced by over 50%. These results are being submitted for journal publication.

This research also included development of a method for experimentally measuring the SAR at various points in the treatment region from the rate of temperature rise in the plastic

sheath of the clinical thermocouple probes currently used for hyperthermia treatment. Results of the experiments show that the probe measurement is dependent on both the angle of incidence of the ultrasound wave and the angle of rotation of the probe. The angle of incidence variation has been documented in the literature, but the angle of rotation variation was a surprise. This variation can be attributed to angularly dependent contact between the thermocouple and the probe sheath. A new probe design has been designed, but has not yet been constructed or tested. Examining the experimental results, it is anticipated that this technique will produce measurement errors of not less than  $\pm 5\%$ .

The results of this project represent a significant step forward in accuracy for a practical, clinical ultrasound power deposition model for hyperthermia treatment planning. The system is currently being implemented on the hyperthermia treatment facility at the University of Utah Hospital and clinical trials are anticipated in future work.

## **First Year Summary**

The first year efforts centered on initial development of the ultrasound propagation models and acquisition and initial development of the diagnostic ultrasound equipment. A brief discussion of these efforts is included below. For more detailed information refer to the first year progress report.

Initial modeling efforts focused on two potential methods: a Green's Function Method where the transducer face is modeled as a distribution of point sources, and the Finite Element Method where FE techniques are used to solve the acoustic wave equation. A two dimensional FE code was written, and verification runs were under way at the end of the first year. The results of these runs and further investigation of the modeling possibilities led to the development of a hybrid model that combines the features of the two techniques to provide improved speed and accuracy. Details of this model are discussed in the second year accomplishments below.

During the first year a diagnostic ultrasound B-mode imager was acquired. This imager was modified to allow access to the raw RF waveform (A-line) for each scan line of the B-mode image. A schematic of the resulting system is shown in Figure 2. The ultrasound unit (Scanner 250, Pie Medical USA 3535 Route 66, Neptune NJ 07753) was modified to output the RF signals along with sync signals. A custom hardware selection device was constructed to read these signals and output a single A-line. A PC based data acquisition system was acquired that allows digitization of the A-line signals. Once the data is in the PC, it is available for use in software techniques to estimate the ultrasonic attenuation field in the tissue. Along with the hardware development, software was developed to operate the hardware and perform the attenuation estimate.[4]

## **Second Year Summary**

### **Subsystem 1: Ultrasound Based Anatomy and Attenuation Measurement**



## Ultrasonic Attenuation Measurement

The power deposited at a specific point in tissue by the ultrasound transducer depends on the intensity of the sound field at that point and the absorption coefficient of the tissue at that point. Clearly, the intensity at a point depends on the initial intensity and the attenuation of the signal in the tissue. This attenuation is due to scattering, absorption, and geometric attenuation. Previous research has shown that the attenuation is highly variable within human body tissue, with measurements varying significantly for different tissue types, for similar tissue on different subjects, and even for the same tissue on the same patient on different days.[6-9] Thus, it is important to measure the attenuation of the ultrasonic signal *in vivo* on the patient at the treatment site.

Using the data acquisition system shown in Fig. 2, it is possible to estimate the attenuation of the ultrasound at different points in the patient tissue from the RF signal collected. This is accomplished using a Log Spectral Difference technique.[7,8,10] Details of this technique are discussed in the second year progress report. It is important to note that Log Spectral Difference is one of several possible techniques and provides an *estimate* of the attenuation.[5] For this reason it is important to test the accuracy of the technique with other measurements.

Tests were conducted where the acoustic attenuation of a series of samples were measured using both log spectral difference and the Force Balance technique. Using the Force Balance technique the force generated when an acoustic wave impinges on an absorbing material is measured and related to the power of the wave. Using this technique it is possible to make a

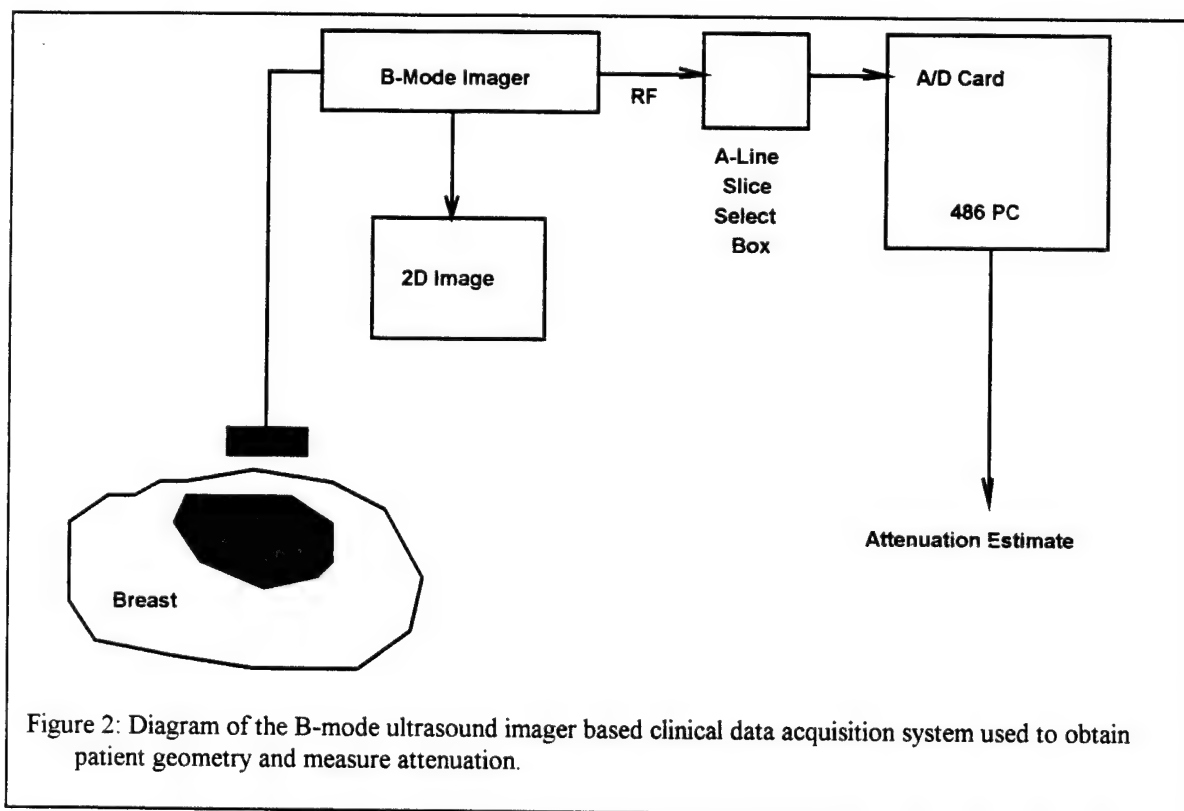


Figure 2: Diagram of the B-mode ultrasound imager based clinical data acquisition system used to obtain patient geometry and measure attenuation.



direct measurement of the attenuation or absorbed power. For this reason, the force balance technique is used as a standard to which the log spectral difference measurements are compared. While it is generally considered accurate and reliable, the force balance technique is not suitable for use in the clinical experiments due to geometric constraints.

Using the techniques described above, initial tests have been run on chicken breast to compare the results of the two techniques discussed above. Using the Log Spectral Difference Technique, the normalized attenuation coefficient for the chicken was measured as  $0.1608 \text{ Nepers} \times \text{cm}^{-1} \times \text{MHz}^{-1}$ . [4] Using the Force Balance system measured values ranged from 0.108 to  $0.138 \text{ Nepers} \times \text{cm}^{-1} \times \text{MHz}^{-1}$ . These values are of the same magnitude as values reported in the literature ( $0.06 - 0.13 \text{ Nepers} \times \text{cm}^{-1} \times \text{MHz}^{-1}$ ). [11]

### **Subsystem 2: Absorbed Power Measurement**

No work accomplished in year 2.

### **Subsystem 3: Ultrasound Propagation Modeling**

During the second year two competing models were developed and compared. The first model was a hybrid numerical model using integral methods to solve for the acoustic displacements in the region where the ultrasound propagates from the transducer to the patient's skin and using a finite element solution of the wave equation for propagation in the body. The model predicts the displacements and stresses propagating through the tissue, automatically accounting for reflections and transmission at all interfaces. This model was expected to be quite accurate. A second model, based on the parabolic equation was also developed. This model accounts for forward scattering and refraction, but ignores reflections. It was expected to be much faster, but it was unclear if this model would provide sufficient accuracy.

### **Results: Hybrid Model**

The Hybrid Finite Element model presented two difficulties:

1. To keep the computational time reasonable, it was necessary to model a relatively small volume. It was not possible to produce boundary conditions at the edge of the volume that approximated free space and the model results included significant standing waves generated at the model boundaries. Expanding the model to include the entire chest cavity would solve this problem, but the model would become unmanageably large.
2. Initial tests were performed at reduced frequency with success. When frequencies corresponding to the treatment transducers were used, the finer mesh required resulted in extremely high computation times.

## Results: Parabolic Model

The parabolic equation method is an efficient method for modeling acoustic wave propagation through low contrast acoustic materials. This solution technique is somewhat more of an approximation than the hybrid model, but because of the geometry used in the hyperthermia experiment, and the relatively low contrast of breast tissue, it is possible to utilize this efficient approximation. The parabolic model was found to be computationally 8 time more efficient than the Green's function model and 64 times more efficient than the hybrid model.

Figures 3 and 4 demonstrate the kind of information available from the models. In Figure 3 we see a continuous plane wave propagating from the left, entering the body through a vertical skin layer. The wave travels through an elliptical fatty region and into the spherical tumor. The top figure shows the wave energy density that tends to get weaker as the wave moves to the right. Note that the tumor absorbs most of the wave energy resulting in a "dark" shadow behind the tumor. The bottom figure shows the energy absorbed. Note that in the water and normal tissue the absorbed energy is low; even when the wave energy is high. There is an increase in absorbed energy as the wave passes into the tumor. This results from the higher absorption coefficient in the tumor. This effect is shown more clearly in Fig. 4 which is a line plot of the absorbed energy along a central axis in Fig. 3.

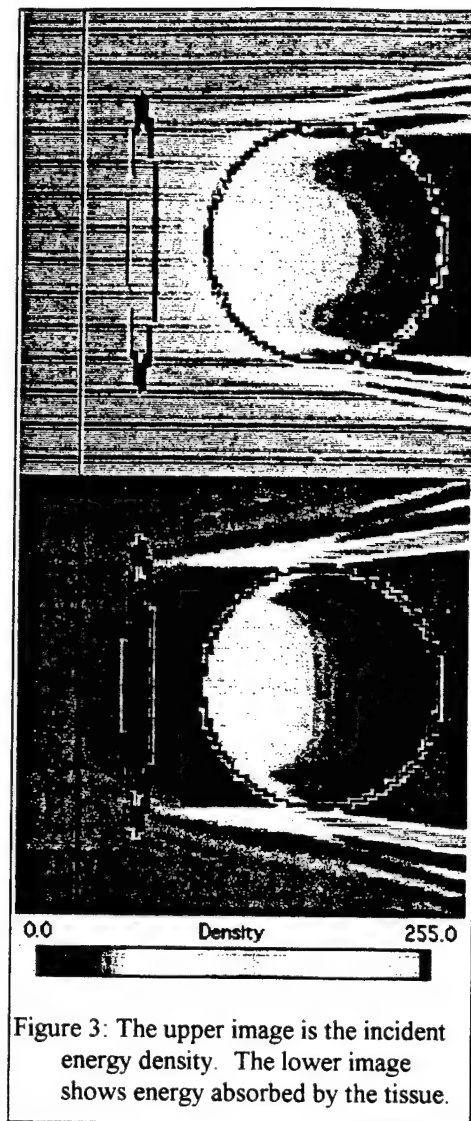


Figure 3: The upper image is the incident energy density. The lower image shows energy absorbed by the tissue.

## Model Accuracy

To test the accuracy of the parabolic method, results were compared to an integral equation solution of the same problem that is representative of the best models currently in use. The following figures demonstrate the agreement between the integral equation method and the parabolic method. Figure 5 shows the geometry used for this analysis. Figure 6a shows a color mapped representation of a slice of the field. Figure 6b is an axial plot of the same data. Figure 7a and 7b show the results using a speed of sound in the sphere significantly

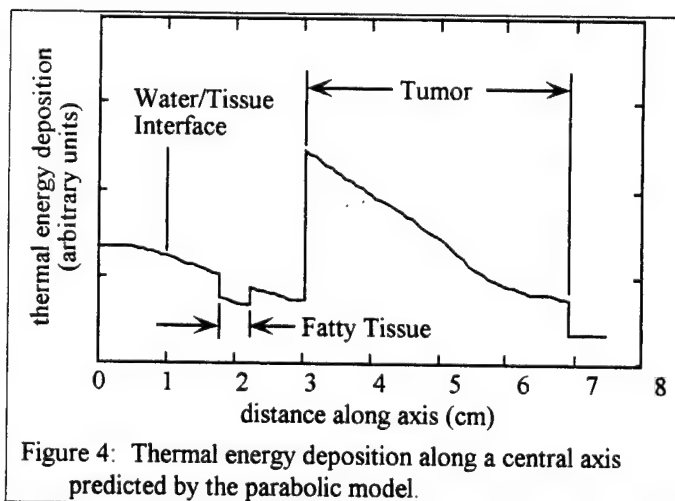


Figure 4: Thermal energy deposition along a central axis predicted by the parabolic model.

less than and significantly greater than that of water. Given the differences in the two models, one would expect error to increase as the mismatch in sound velocity between the tumor and water increases. Thus, these two conditions should represent worst case errors.

The excellent match between the two models in the forward scattered diffraction patterns shown in Fig. 7 and the poor match in the reflected diffraction pattern shown in Fig. 6b highlight the differences between the two models. The excellent overall match between the two models in these worst case conditions, coupled with the speed provided by the parabolic model make it an excellent candidate for our application.

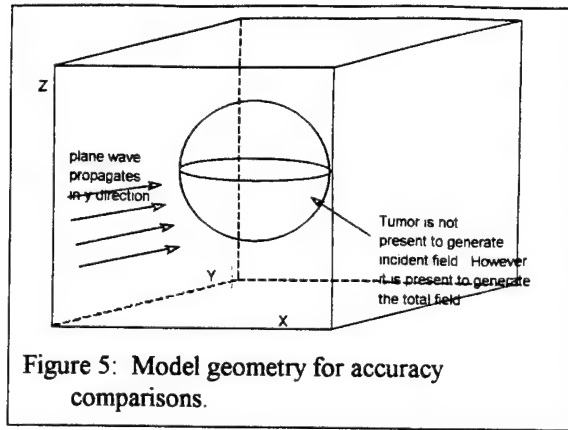


Figure 5: Model geometry for accuracy comparisons.

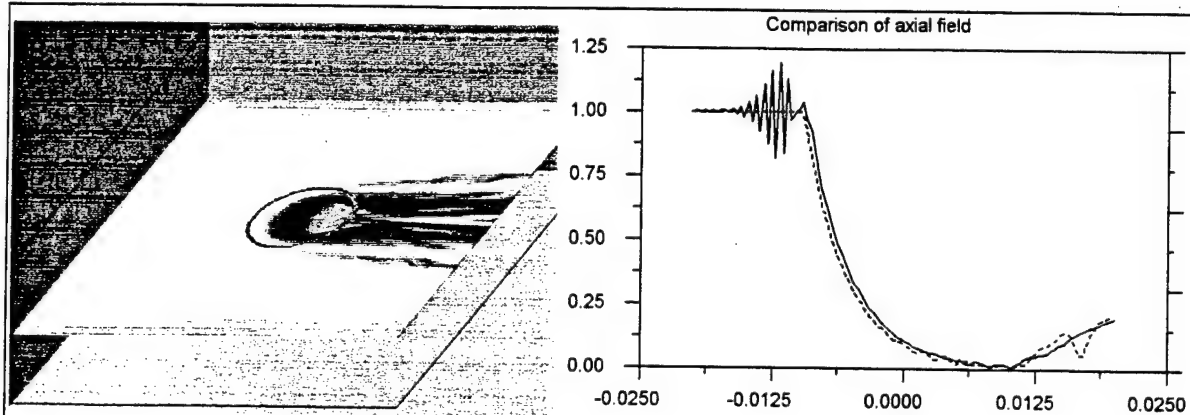


Figure 6: a) Color mapped image of the power deposition in the model from Fig. 5. b) The integral equation is shown in solid, and shows the diffraction pattern due to reflections from the hard sphere. This plot shows quantitatively that the parabolic method does not take into account the reflections of sound waves. Conditions for this graph correspond to those in Fig. 7b.

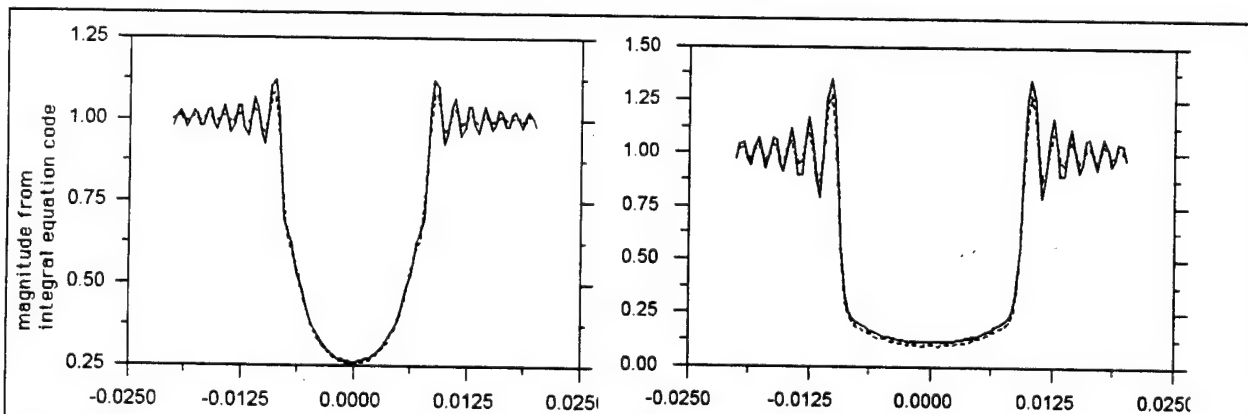


Figure 7: a) The speed of sound internal to the sphere was 1267.7 m/sec, substantially less than that which would be encountered in the breast, thereby making the impedance contrast quite a bit larger than is likely to be encountered in practice. b) Here, the speed of sound internal to the sphere was 1677 m/sec, which is substantially greater than any tumor that would be found in the breast. In each case the solid line represents the integral model and the dashed line represents the parabolic model.

#### Subsystem 4: Inverse Optimization Technique

No work accomplished during the 2nd year.

### Third Year Summary

#### Subsystem 1: Ultrasound Based Anatomy and Attenuation Measurement

- Laboratory hardware was developed to provide 3D scanning capability for the medical B-scan imager.
- Software to produce a 3D, tissue attenuation map from the A-mode signals was completed.
- Software and hardware for clinical patient geometry approximately 50% complete.

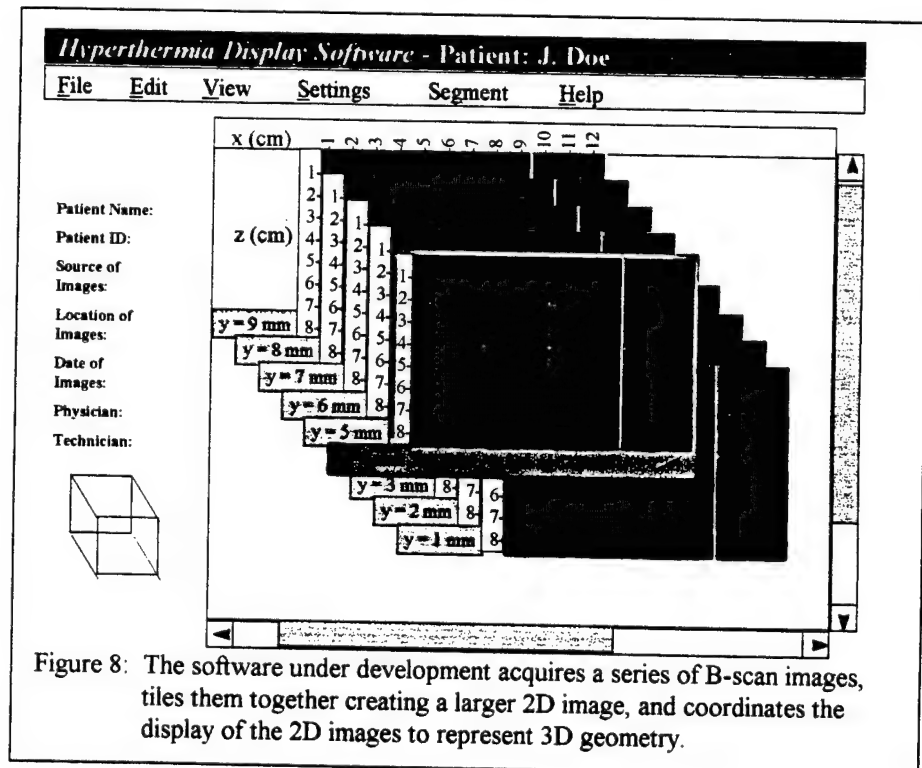
#### Patient Geometry Acquisition and Registration

The goal here is to be able to place a patient in a known, repeatable location on the treatment station and, using the B-scan imager, identify the geometric structure of the tissue and tumor in the region under treatment.

#### Clinical System Description

The patient positioning system consists of several integrated steps. The first step is a repeatable patient positioning system. While concepts were developed during this year, no final design or construction were completed.

In the second phase of positioning the patient, a series of B-scan ultrasound images of the treatment area are collected. These images are used to identify the locations of thermocouples, interfaces between different tissue types, and other anatomical features within the region that will be affected by the hyperthermia treatment. The B-scan images are digitized using a video capture card. A custom software, developed as part of this research,



coordinates multiple B-scan images into a series of slices representing the 3D patient geometry. A screen capture from this system is shown in Figure 8.

The doctor or technician traces features of the B-scan images that are of interest. Using an attenuation map developed using a process described below as a reference, the different regions identified by the tracings are assigned attenuation values. The software processes this information and produces a 3D grid of nodes where each node is assigned appropriate values to represent the patient geometry for processing by the math model. Figure 9 demonstrates this process.

The left most image contains 3 B-scans that have been registered and combined, producing a single image. In the center image, the doctor or technician has mouse sketched different regions. In the right most image, these regions have been assigned different acoustic properties based on apriori knowledge and information from the attenuation mapping system discussed below.

The following outline describes the anticipated clinical procedure using the developed system. Depending on the time required to complete the inverse optimization procedure, the patient may either lay in position and wait, or be released and return for treatment hours or days later.

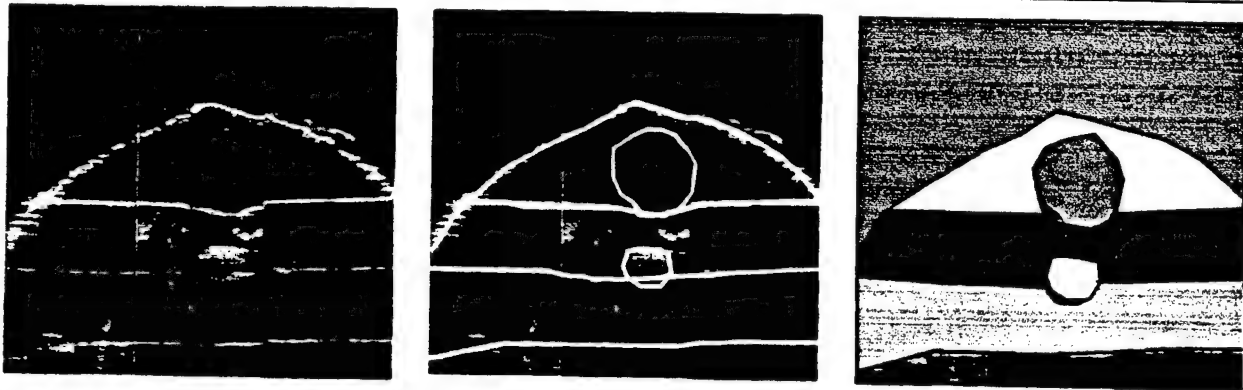


Figure 9: Each image is processed by a doctor or technician. The process involves mouse sketching the borders of identifiable regions and assigning each region uniform acoustic values estimated from an attenuation map.

## **Three-dimensional Ultrasonic Attenuation Field Measurement**

As mentioned above, the goal of this research is to produce a model that will accurately predict the power deposited at all points in a region of tissue, during a hyperthermia treatment. This will allow the physician to develop a better treatment plan that will maximize the positive effects and minimize pain and other adverse effects. In order for the inverse model to accomplish this efficiently, the model must begin with model parameters that are "in the ball park" of the final optimal values. The least well known of these parameters is the acoustic attenuation of the tissue. Thus, a technique was developed that predicts the acoustic attenuation field within the tissue based on data from a B-scan imager. The third year efforts extended the previous accomplishments to include the ability to produce a 3D attenuation map from a series of B-scan images.

### **Background**

Measurement of ultrasonic attenuation from reflected signals has shown promise of being a valuable diagnostic tool [12-20]. It allows physicians to diagnose illnesses that cannot be diagnosed on a B-mode ultrasound image. Because of this, several methods of calculating the ultrasonic attenuation from reflected signals have been developed [14,17,19-22]. These methods were then used to calculate the global attenuation of a structure. The next step in attenuation calculation was to produce an attenuation image that could be used in conjunction with the B-mode image. Walach and others have developed techniques that relate a two-dimensional B-mode image to a two-dimensional attenuation image or map [12,13,23]. Seeing both images side-by-side, the physician has an increased diagnostic capability.

However, the usefulness of an attenuation map is not limited to diagnostics. A 3D attenuation mapping technique has been developed here that not only provides the initial estimates for the power deposition model. But has potential to produce enhanced resolution 2D attenuation images.

### **Method**

In order to build the three-dimensional attenuation map, a B-mode imaging transducer was placed on a two-dimensional linear motion machine. The transducer is part of an ultrasonic imaging system (PIE Scanner 250) which provides access to the reflected ultrasound signal (A-line), before processing, as well as synchronization signals to give the location of the waveform along the width of the transducer. With this in place, software was developed that scanned the transducer to cover the entire geometry of the structure being modeled, while collecting and organizing the data. This is the same data shown in Figures 8 and 9 collected by the patient registration system, except that the raw A-lines are recorded.

The data was collected with an eight-bit analog to digital converter, and was then written to disk. A technique has been developed that uses several different gain settings for each collection to mimic a higher-precision conversion. Using this technique, each A-line was analyzed at the highest possible gain setting where saturation did not occur. The focus of the transducer was set so that the structure being analyzed was in the far field of the transducer. This insures that diffraction effects in the near field do not enter into the calculations. Once the data was collected it was then analyzed to produce the attenuation map.



The log spectral difference method was used to estimate the slope of the attenuation to frequency relationship. (Lyons and Parker found that for most soft tissues, the attenuation was related to frequency to the power of  $n$ , where  $n$  is equal to 1.0 - 1.3 [25]. The value for  $n$  was set to 1 in this research.) This method utilizes the ratio of the power spectrum from a shallow and deep segment of the region of interest (see Figure 10) to compute the attenuation slope for that region. The specific steps of this technique have been presented in the 2<sup>nd</sup> year progress report as well as previously in the literature and will not be discussed here [14,15,22,26]. Our application of this method for the production of a 3D, attenuation map will be discussed next.

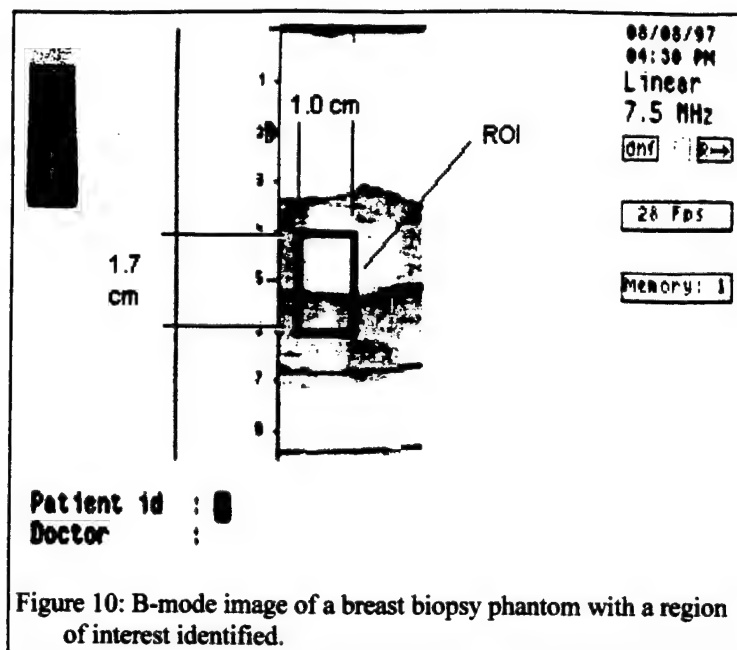


Figure 10: B-mode image of a breast biopsy phantom with a region of interest identified.

As mentioned previously, the log spectral difference technique is a way of estimating the slope of the attenuation for a specified Region Of Interest (ROI). To produce the attenuation map, a ROI of a determined size was moved throughout the three-dimensional data space until an attenuation map was produced. The region of interest selected was 1.0 cm wide and 1.7 cm in depth (see Figure 10). The width was chosen because it allowed the computation to be averaged over ten reflected signals. The depth for the region of interest came from a formula presented by Kuc [26] and the specifications of the transducer. Once the ROI size was selected, it was moved throughout the data space incrementally in 1.0 mm steps in all three directions. The attenuation-slope value for each calculation was assigned to a point in the center of the ROI, thus producing an attenuation map. This 2D ROI is similar to that used by previous researchers. The additional information available from the 3D data collection used here allows a 3D ROI to be investigated, where data from a 3D region are averaged together to improve the accuracy and/or resolution of the measurement. Software has been developed to

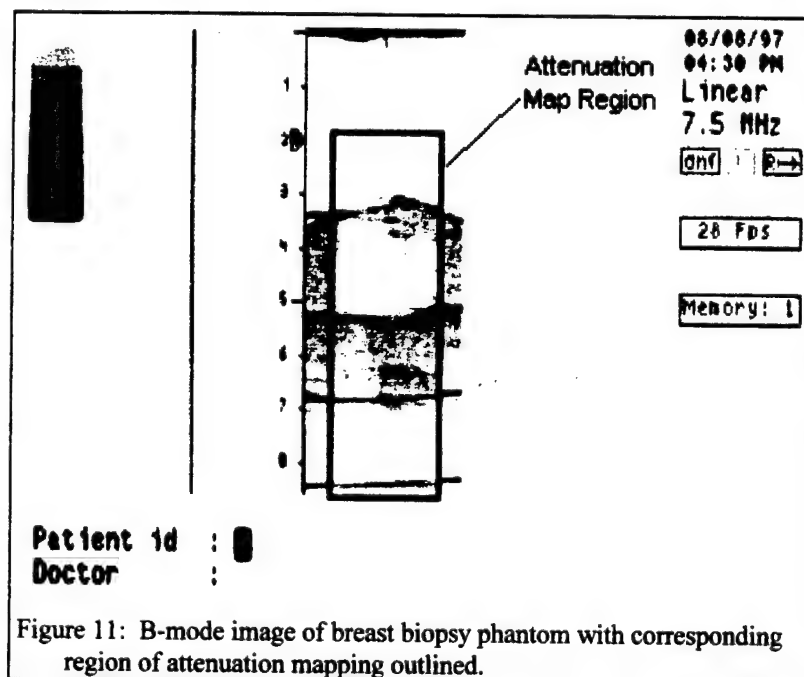


Figure 11: B-mode image of breast biopsy phantom with corresponding region of attenuation mapping outlined.

completely automate the task of data acquisition and analysis, and calibration tests are underway.

## Results

Various tests have been performed to determine the settings that produced the most precise and least noisy attenuation map. Initial tests varied the ultrasound power, gain setting, and whether or not the region of interest should be two-dimensional (space averaged) or three-dimensional (volume averaged). For these preliminary experiments, visual comparison of the attenuation images versus the anticipated attenuation image (obtained from examining the B-mode image) was used to determine the optimal settings.

Preliminary results showed no benefit from the 3D volume averaging. During the analysis of the attenuation images, it was noted that data was lost in areas where the ultrasound back scatter was too low, or too high. For any single gain setting, the data loss was significant. However, based on a visual comparison, other gain settings appeared to produce attenuation images of the almost the same quality, but with data losses in different regions. These observations resulted in the multiple gain setting technique discussed above. This technique resulted in images with significantly less data loss.

Figure 11 presents a B-mode image of a breast biopsy phantom. This image was taken at the same time that attenuation data was being acquired for the same image space. Because the attenuation slope value is assigned to a point in the center of the ROI, and the because of the size of the ROI, 0.5 cm of attenuation data was lost on each side of the B-mode image. For the same reason, 0.85 cm was lost from the top and bottom of the image. Figure 12 shows the corresponding attenuation map for the region indicated in Figure 11.

## Discussion

Attenuation maps are not a new application. Walach and others have produced attenuation maps in the past [12,13,23]. However, this application is the first three-dimensional mapping system we have been able to find. This application has limitations similar to the other maps that have been produced. One such limitation is the resolution of the attenuation map.

Most attenuation-calculation techniques require a large ROI in the depth direction. The literature has recommended that the log spectral difference method be used for global attenuation estimation (greater than 5.0 cm) [14,22]. However, Kuc has theorized that this method can be used for smaller regions, but that the size of the ROI has a lower limit. As the length of the ROI decreases below this limit, the noise associated with the application increases dramatically [26]. As can be seen from Figure 12, the resolution is poor compared to the B-scan image. In addition, the attenuation image only partially matches

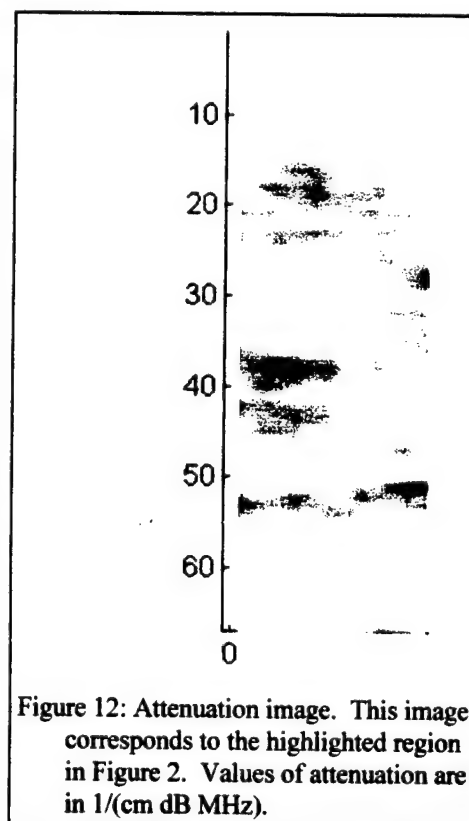


Figure 12: Attenuation image. This image corresponds to the highlighted region in Figure 2. Values of attenuation are in  $1/(\text{cm dB MHz})$ .



the expected image (from examining the B-mode image in Figure 11).

Inhomogeneous regions are another problem with this technique. Several interfaces and varying structures were present in the phantom that was used for calculation. The development of this and other estimation techniques were based on the tissue being homogeneous within the ROI [14,17,18,21,22]. This problem was initially ignored in this study in order to discover how the method would handle interfaces and different tissues within the ROI. The bright circle in Fig. 11 is a water filled sphere, 1.2 cm diameter. Note that while this sphere is smaller than the ROI it does show up. This is taken as a sign that this method may be used to calculate the attenuation in small tissue structures.

Another source of error in the three-dimensional map is the location error of the transducer. In tests, the largest error in positioning the transducer found was 0.04 mm. The beam width of this transducer at the focal point is 1.4 mm. Therefore, the positioning error is not considered a significant source of error.

Regardless of the errors involved, the attenuation estimation method should be successful if it can appropriately predict the relationship between the attenuation and the various structures within the phantom or anatomy. (i.e. which regions have "higher" attenuation and which regions have lower attenuation.) This kind of an approach can be taken because of the iterative nature of the inverse model that will use these values.

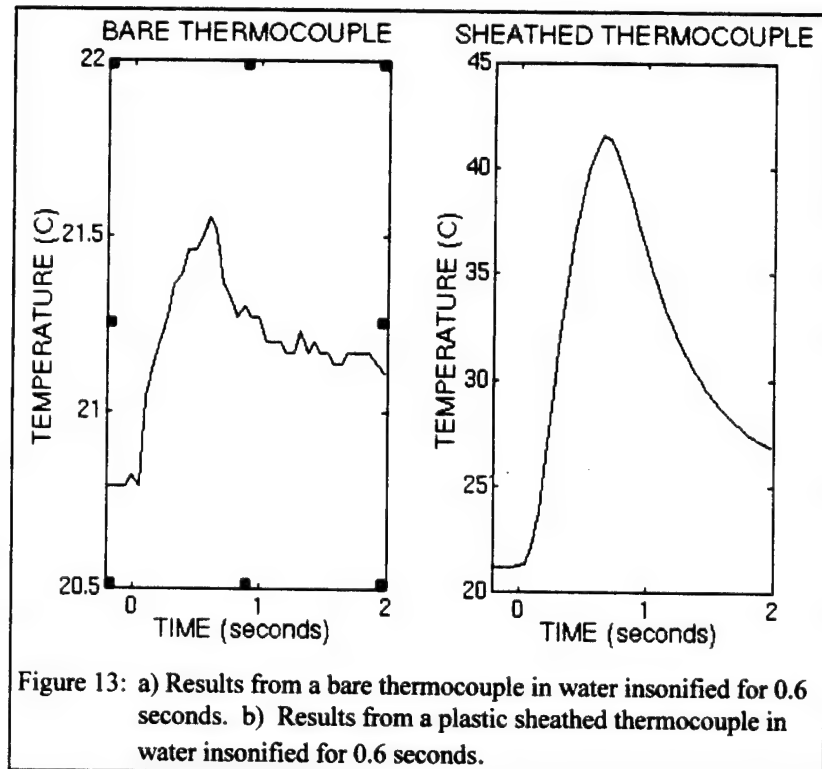
## **Subsystem 2: Experimental SAR Measurement**

- Thermocouple based beam plots have been performed to calibrate the ultrasound power field in water for specific transducers.
- Experiments have been conducted in water and will begin shortly using cast agar phantoms.
- Preliminary in-vivo experiments were conducted on a dog.
- A finite difference model has been constructed to help interpret the experimental measurements

To accomplish the inverse optimization of the theoretical model, the results of the model must be compared against actual values that are determined by experimental means. The ultrasound propagation model predicts the incident power at all points in the modeled region, as well as the absorbed power. At a given point, these two quantities are related through the local attenuation. Thus, the model can be optimized by comparing the propagation model results to either the incident power or the absorbed power at several points in the model. The experimental values needed for optimization can be determined using the same thermocouples which are inserted for observation of steady state temperature during clinical hyperthermia treatment.

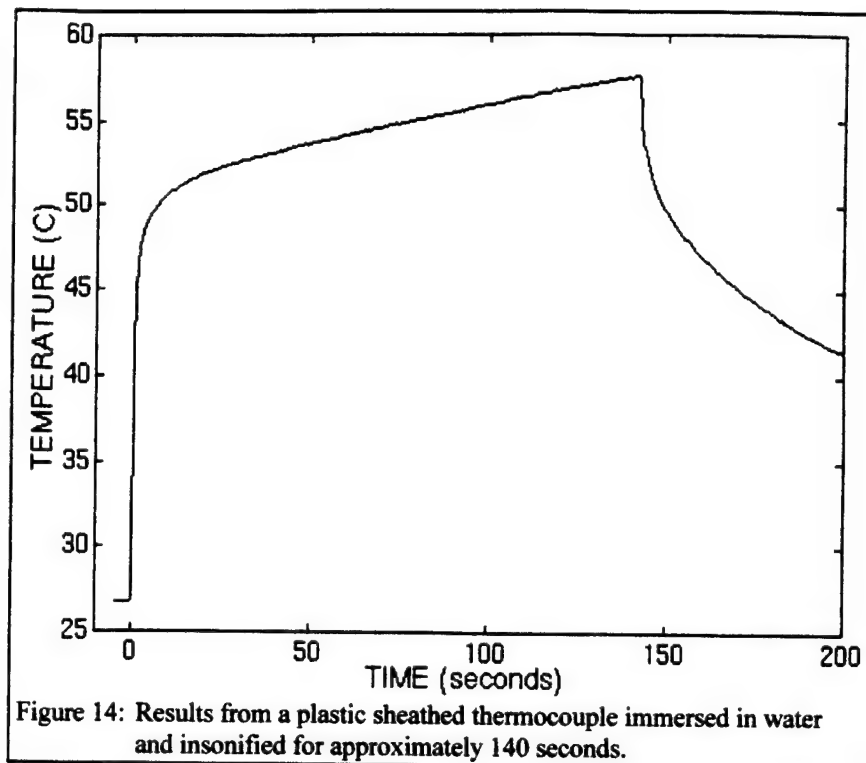
Experimental measurement of the power deposited in tissue at a specific point is not entirely straight forward. Researchers note that the interaction of the thermocouple probe with the ultrasound results in temperature artifact.[24] This artifact results from two sources: viscous heating at the interface between the probe surface and the tissue, and absorption of acoustic energy by the probe its self. The viscous heating is a surface phenomena and results in a small artifact with a short time constant causing a rapid initial temperature rise when acoustic power is initiated. This artifact is usually only noticed when conducting tests using bare thermocouples. Probe sheaths of steel, fused silica, and various plastics have been shown to absorb ultrasound power at a higher rate than tissue. Plastics, the most common sheath materials used in hyperthermia treatment, absorb ultrasound energy at a significantly higher rate than tissue resulting in a significant artifact that is exhibited over a longer time scale than the viscous artifact. The temperature rise in the tissue, a much larger volume than the sheath, occurs over an even longer time scale.

The combined result of these effects is shown in Figure 13. In Figure 13(a), a bare thermocouple was submersed in a water bath and insonified for 0.6 seconds. Note the rapid initial jump followed by a relatively linear region. The initial jump is caused by viscous heating at the thermocouple/water interface and the linear region is established when local conduction between the thermocouple and surrounding water becomes significant. At longer times the temperature rise will become non-linear as larger scale conduction and convection become significant. In Figure 13(b) the experiment was repeated with a sheathed thermocouple. Note that the temperature rise is much more significant, rising roughly 20 degrees in 0.6 seconds compared to less than one degree for the bare thermocouple. This large jump is attributed to the power absorption of the sheath. Any viscous heating that occurs is clearly lost in this rapid temperature rise. The slope of this rise is indicative of the power absorption in the sheath.



If the power is applied for a longer time, the rapid initial rise of the sheathed thermocouple is balanced by conduction between the sheath and the surrounding water. This effect is shown in Figure 14. The second linear regime achieved represents the temperature rise of the media surrounding the thermocouple.

In these experiments the thermocouples were immersed in water, a very poor absorber of ultrasound energy. Thus, essentially all of the temperature rise of the water was due to conduction from the



thermocouple sheath. In tissue we expect larger absorption directly by the tissue. An actual experiment conducted in tissue will produce results similar to those shown in Figure 15. Here a sheathed thermocouple was inserted in the muscle tissue of the thigh of a dog. The focus of the ultrasound transducer was centered on the thermocouple and the area was insonified for 0.6 seconds at several different power levels. Note that in each case the power was much lower than that used in the experiment from Figure 14, evidenced by the relatively low temperature rise. In future experiments we intend to calibrate the plastic sheath and use it as an incident power sensor, allowing the ultrasound power incident at the thermocouple to be measured.

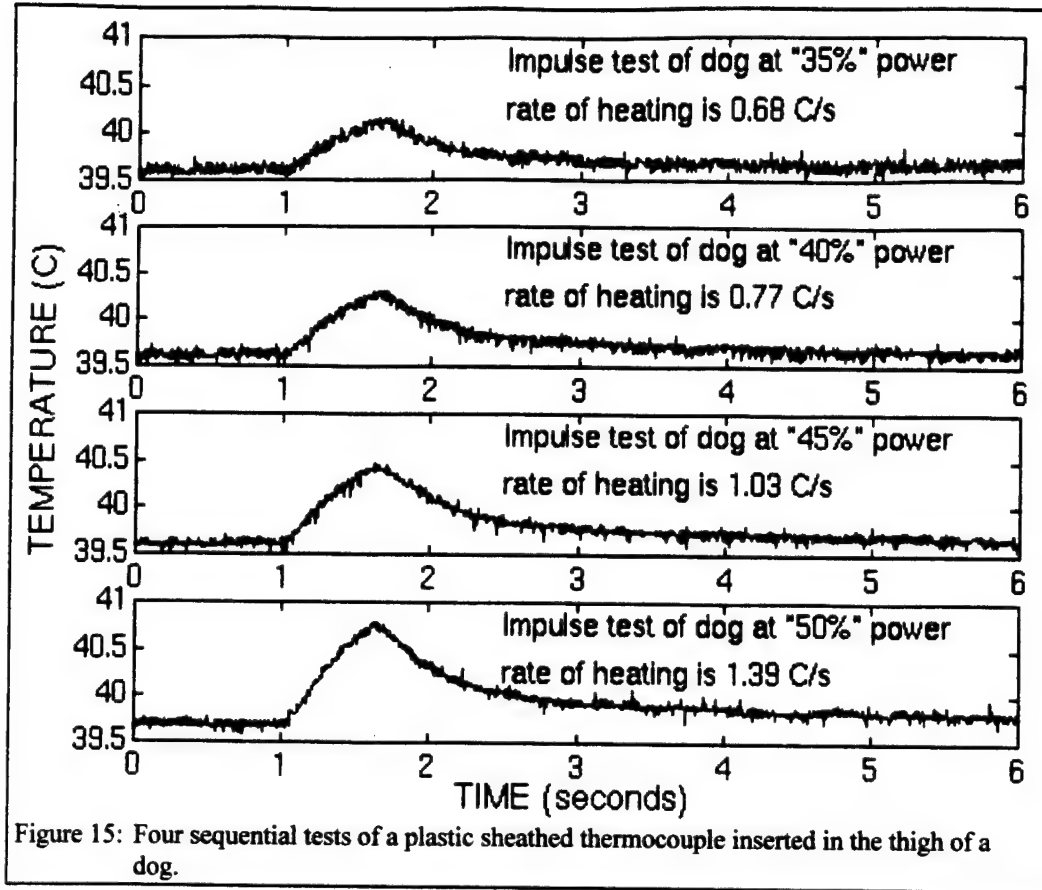
### Modeling the Thermocouple Behavior

In the absence of conduction, power is related to heat generation by the following equation:

$$\rho_p \frac{dT}{dt} = \alpha I \quad \text{Equation 1}$$

where  $\rho$  is the density,  $c_p$  is the specific heat,  $\alpha$  is the absorption coefficient, and  $I$  is the local intensity of the ultrasound field.

If a plastic thermocouple probe and surrounding tissue at uniform temperature is suddenly insonated by ultrasound of constant intensity, the probe and tissue will begin to rise in temperature. The plastic probe will heat more rapidly than the tissue because it has a larger absorption coefficient than the tissue. For a short period of time immediately following insonation, conduction of heat will be small and the rate of temperature rise is dependent solely on the absorption coefficient of the medium being insonated. If the time constant of the thermocouple is sufficiently small the thermocouple, being surrounded by plastic, will reflect the



temperature of the plastic. If the absorption characteristics of the thermocouple probe can be sufficiently characterized, the intensity of incident ultrasound can be determined by the temperature vs. time response of the thermocouple to a suddenly applied ultrasound field.

The radial distribution of a focussed ultrasound beam can be closely estimated as a Gaussian function. The following equation describes the radial intensity distribution:

$$I(r) = I_{\max} e^{-r^2 / \beta} \quad \text{Equation 2}$$

where  $I_{\max}$  is the intensity at  $r = 0$  and  $\beta$  is a measure of the beam width as determined by a least squares error curve fit. [24]

If the ultrasound is applied for a short duration to prevent significant conduction effects then the temperature distribution produced by the absorption of the ultrasound will also be Gaussian. Using the theory put forth by Parker, the time dependent temperature at the center of the focal region can be described by the following equation:

$$T(t) = T_{\max} / (4kt / \beta + 1) \quad \text{Equation 3}$$

where  $k$  is the heat conduction coefficient of the tissue and  $T_{\max}$  is the maximum temperature attained at the center of the focal region at the end of ultrasound application.

At the termination of the momentary application of ultrasound the plastic sheathing of the thermocouple probe will be at a higher temperature than the surrounding tissue. However, because the heat capacity of the thermocouple is small compared to the heat capacity of the tissue, excess heat stored in the probe will diffuse into the tissue and the probe temperature will reach equilibrium with the surrounding tissue and follow the temperature decay of the surrounding tissue. Curve fitting the decay of the tissue temperature by the least squares error method the decay can be backtracked and the value of  $T_{\max}$  determined.  $T_{\max}$  and the duration of insonation are used with equation (1) and the intensity determined by the rate of heating to determine the absorption coefficient of the tissue.[24]

It has been determined by previous investigators that absorption accounts for 90-100% of attenuation in soft tissue.[25] Therefore it is not completely accurate to compare attenuation determined by B-mode imager and absorption determined by thermocouple probe but an error less than 10% is not unreasonable when compared to other errors likely to exist.

A program was created on the hospital treatment system that positions the transducer, delivers power for a period of time, and records the temporal temperature data from the thermocouple probes. This program is able to attain temperature data from several seven junction probes every 3/100 sec. To test the program a 10 cm, 2MHz transducer was mounted to the positioning gantry and an array of thermocouples was placed in a water bath above the treatment system. The thermocouples were located with the existing thermocouple locate routine. It was found that the positioning system was only able to locate the thermocouples with  $\pm 2$ -4cm accuracy. A radial beam intensity plot was attempted beginning 1 cm away from the center of focus and traversing through the focus at 2mm increments. Because of the tight beam focus and lack of positioning accuracy it was found that there was very little correlation between expected position and beam intensity.

To characterize the beam shapes of the available transducers, an array of epoxy covered thermocouples was created and oriented perpendicular to the beam axis. The array was moved through the beam transverse to the beam axis in 1mm increments and the steady state temperature was recorded for the thermocouples at several different distances from the face of the transducer. This procedure was followed for the focussed 10cm diameter 2MHz, focussed 7cm diameter 500kHz, unfocussed square 4cm 1MHz, and unfocused 3cm diameter 4MHz transducers. The unfocussed transducers were not characterizable because of the irregular intensity consistent with the long near field of the beams. The 10cm and 7cm diameter transducers had a Gaussian profile in the radial direction at the focus. Least squares error curve fit produced a Gaussian parameter of  $0.029 \text{ cm}^{-2}$  for the 10 cm diameter transducer and a Gaussian parameter of  $.42 \text{ cm}^{-2}$  for the 7cm diameter transducer.

The  $0.029 \text{ cm}^{-2}$  Gaussian parameter at the focus of the 10cm diameter transducer creates a beam width of around 6mm. which is too narrow for the accuracy of the hospital positioning system and the steep temperature gradients created by the narrow focus decrease the temporal window during which conduction is insignificant. The  $0.42 \text{ cm}^{-2}$  Gaussian parameter at the focus of the 7 cm. diameter transducer creates a beam width larger than 2 cm. This larger beam width will create a less steep temperature gradient and lengthen the temporal window for the rate of heating measurement. The longer length of focus of the 7 cm. transducer is also beneficial in avoiding error in the Z-direction.

Finite difference code was written to model a thermocouple probe embedded in tissue. The finite difference model will be used to verify the assumptions and clarify the unknowns of the experimental technique. Verification of the 1-D model is in process after which a 2-D and/or 3-D model will be created.

A considerable amount of phantom testing with the 7cm. diameter transducer will begin shortly. The phantom tests will be designed to prove the accuracy of the rate of heating and thermal pulse decay technique in combination with the probe geometry used in clinical hyperthermia treatment. After verification the procedure will be integrated with the other subsystems of the inverse estimation technique to provide geometric data for the thermocouple probes and local measured power and absorption values.

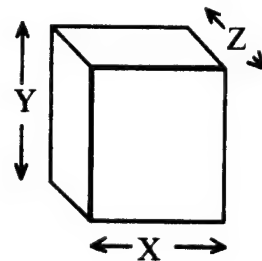
### Subsystem 3: Model Development

- The parabolic model has been selected for use in regions of low acoustic contrast. In these regions the model is quite fast and loses little accuracy when compared to the Green's Function Model. The Green's Function Model can be used in high contrast areas (close to ribs, etc.)
- An interface has been built for the model which allows the user to specify the volume modeled, the acoustic power input as a 2D complex pressure function, and the model parameters; density, sound velocity, and absorption at each node within the volume.

Based on the results of the 2nd year, the parabolic model was selected for use in regions of low acoustic contrast. In these regions the model is quite fast and loses little accuracy when compared to the Green's Function Model. If necessary, the Green's Function Model can be used in high contrast areas (close to ribs, etc.) The Green's Function Model could be used everywhere resulting in a significantly slower, slightly more accurate result.

During the third, year work on the model focused on the development of a practical and convenient user interface that allows the model to be adapted to different transducers and tissue geometries. Toward this purpose, an interface was built for the model which allows the user to specify the volume modeled, the acoustic power input as a 2D complex pressure function, and the model parameters, density, sound velocity, and absorption at each node within the volume. The model interface, as described below is complete.

The interface allows the user to specify the dimensions, X, Y, Z of a rectangular volume that will be modeled. The size of the volume to be modeled is limited by the requirement for 2 nodes per wavelength at the transducer frequency under investigation and by the maximum number of nodes that the model can handle. At the current time, the model can handle 1,000,000 nodes. Thus, a volume of 100 by 100 by 100 nodes could be modeled. At 1.5 MHz, this would be a 5 cm cube. It should be noted that larger volumes can be modeled by slicing the volume into 1,000,000 node rectangles and modeling each sequentially.





Within the modeled volume the tissue is characterized by specifying the density, sound velocity, and acoustic absorption at each node. As a result the interface is very general. There is much more flexibility in this interface than is currently required by the inverse optimization scheme. If we later desire to optimize the sound velocity field within the tissue, or the density field, no modifications to the model will be required.

### Transducer Model

If the transducer were modeled as part of the above described volume, it would be difficult to fit the desired tissue volume into the limited model volume. This problem is addressed by solving for the complex pressure field created by the transducer being modeled and applying this field at one surface of the model volume.

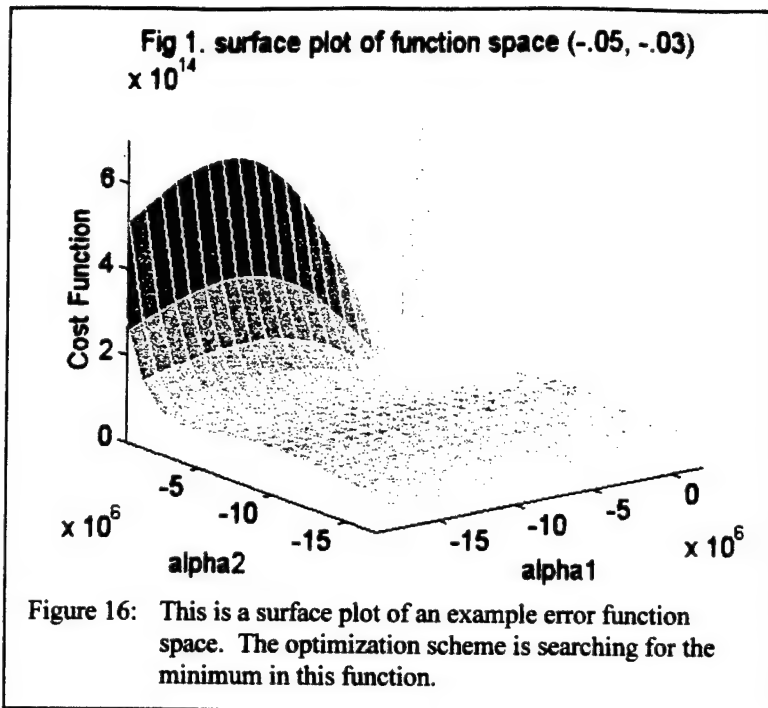
The 3D complex pressure field is first found for the transducer in water. This is done by matching a numerical solution to the results of calibration experiments where the temperature rise of epoxy coated thermocouples is measured in a water bath. Using this data, as long as the edge of the modeled volume extends beyond the skin into the water bath, the effects of the transducer can be modeled accurately by finding the intersection between the planar surface of the model and the 3D pressure field. Note that a single calibration allows the transducer to be positioned anywhere with respect to the model volume.

With this user interface in place, the model can be treated as a black box, where the optimization scheme is ignorant of the details of the model within the box, but simply specifies inputs and collects the output from the model. Once the transducer has been calibrated (or several transducers), the user simply specifies the transducer location and orientation, and the nodal acoustic properties that were identified in Subsystem 1. The model then outputs the acoustic power deposited at each node within the model volume.

### Subsystem 4: Inverse Technique

- Basic algorithm development is complete. Optimization runs have been completed on simple geometries.

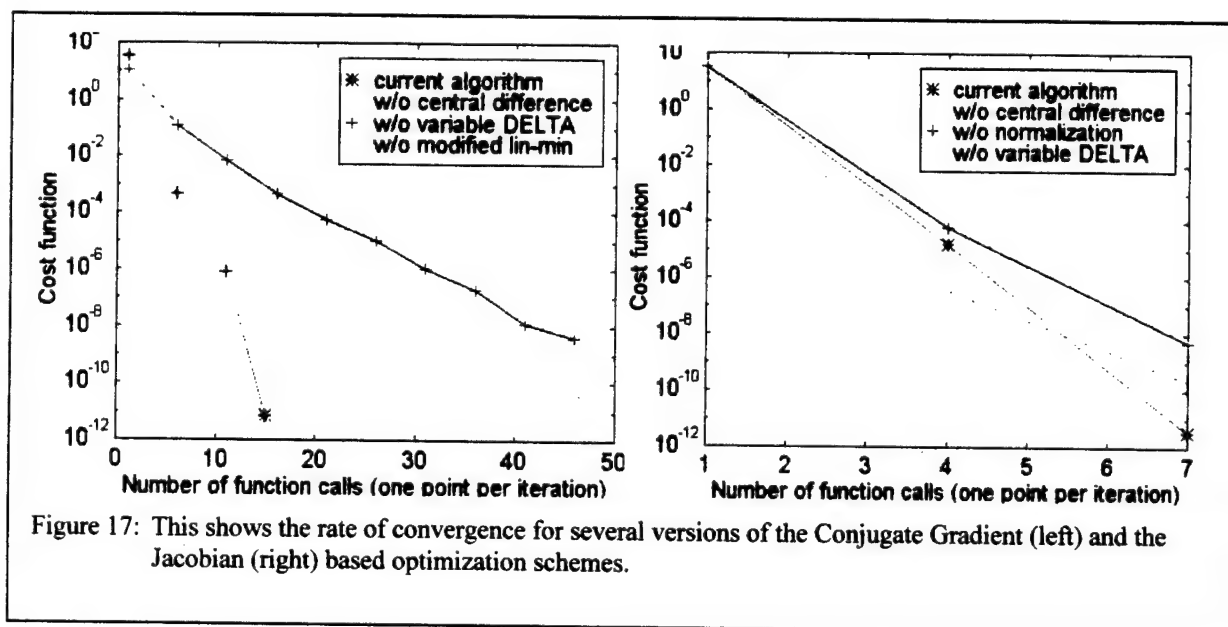
### Inverse Method for Optimizing Tissue Attenuation Values



In the original proposal, it was suggested that three parameters could be allowed to vary between tissue types. The numerical model developed has the capability to change all three parameters. However, in initial trials, it is assumed that speed of sound, ( $c$ ) and impedance, ( $Z$ ) are known constants for the tissues with which we will be dealing. Consequently, attenuation is the only parameter that changes between tissue types and, thus, will be the only parameter optimized.

The method discussed in the proposal uses the Jacobean matrix to adjust the initial parameter values at model nodes and iterates until the error function is minimized. (Here error is some weighted sum of the differences between model predictions and experimental measurements.) This method was used in initial trials and then compared to other methods. A second method, the Conjugate Gradient method, was also evaluated.

Trials were completed using each of these methods to search for minimum error points in the error function for simple function spaces. Figure 16 shows an example where only two parameters are varied. Given an initial value for the two parameters, each method iteratively searches for the optimum (minimum) point in the function. Essentially the only difference between the various optimization schemes is the efficiency with which they "slide down the hill" to find the minimum value. This efficiency is based on the number of function calls (forward model iterations) required to produce one optimization iteration, and on the number of optimization iterations required to reach the minimum error. Figure 17 shows trials using both the Jacobian and the Conjugate Gradient methods for optimization.





## **Fourth Year Accomplishments:**

### **Subsystem 1: Geometry Acquisition and Attenuation Measurement**

- **Verification tests for clinical system for 3D attenuation mapping.**

The hardware and software for the attenuation mapping system were completed by the end of the third year of the project. During the fourth year, validation tests were performed. These results will be reported quite briefly here. Detailed results can be found in [27].

In this work a modified ultrasonic B-mode imaging system was combined with a two-axis motion device, making it possible to collect a series of raw, reflected ultrasonic wave forms that represent a three-dimensional volume. The attenuation coefficient for a specific region of interest (ROI) was estimated using the log spectral difference technique. In order to reduce the level of noise in the attenuation estimate, a region of interest was specified within which the estimates were averaged. Using experimental data collected from graphite/agar phantoms the minimum size ROI that will produce a reliable signal has been investigated. The results show that a 2D ROI, where information is taken from a region within a B-scan, must be approximately 2.5 cm in the depth direction by 1 cm in width to produce a reasonable signal. Information combined from adjacent B-scans into a 3D ROI can reduce the apparent size of this region within the 2D plane by improving the lateral resolution. In this case, the minimum ROI was identified as 2.5 cm (depth) by 5 mm by 5 mm.

### **Methods**

A clinical B-mode imaging system and a two-axis motion machine were used to acquire reflected ultrasound signals from a graphite/agar phantom in three dimensions. Then, the log spectral difference technique was used to calculate the local attenuation coefficient. The accuracy of the attenuation measurements was verified with a force-balance calculation of attenuation made from the phantom. Details of the system and the attenuation calculation techniques have been presented in previous reports and will not be presented here. The following sections present the methods used to acquire and analyze the results.

### **Data Acquisition**

Preprocessed, reflected ultrasound signals were acquired from a modified clinical imaging system and a two-axis motion system. In order to produce 3D results, multiple slices of a-lines were acquired on a symmetric 2D grid. Each slice of data corresponded to the B-mode image produced by that data. Individual a-lines acquired within each slice were spaced 1 mm apart (x direction). Slices were spaced 1 mm apart in the direction orthogonal to the spacing between a-lines within a slice (y direction). The final dimension came from the reflected signal itself (z direction or depth). Acquisition of the signals in this manner was accomplished by fixing the imaging transducer to a two-axis motion system, moving the transducer, and acquiring the signals.

The signals were acquired while the transducer was scanned across a homogeneous graphite/agar phantom. A layer of water was used as the acoustic pathway to couple the imaging transducer and the phantom. In order to produce a standard to compare with the attenuation measurement system results, the same graphite/agar solution used to make the

imaging phantom was also used to make two force balance phantoms. Each force balance phantom had a different constant thickness. Therefore, an attenuation coefficient could be calculated from force balance tests. In addition, the calculated coefficient from the force balance could be used to determine the accuracy of the attenuation measurement system.

### Data Analysis

The log spectral difference method was used to estimate the slope of the attenuation to frequency relationship [14, 15, 22, 4]. This method utilizes the ratio of the power spectrum from a shallow and deep segment of a reflected ultrasound signal to compute the attenuation slope for that region. Once the slope has been calculated, the normalized attenuation coefficient can be computed by using Equation 4. In this equation  $\beta$  is the normalized attenuation coefficient

$$\beta = \frac{\omega}{2D}$$

Equation 4

(normalized to depth and frequency),  $\omega$  is the slope of the log spectral difference, and  $D$  is the distance between the shallow and deep segments and is equal to two-thirds of the specified ROI depth. In order to compute an attenuation coefficient, the relationship between attenuation and frequency is assumed to be linear, and at zero frequency the coefficient is assumed to be zero. Therefore, the calculation of the attenuation coefficient ( $\alpha$ ) can be easily calculated by using Equation 5, where  $f$  is the frequency. Since the attenuation coefficient is frequency dependent, all values reported in this paper are at a frequency of 1.0 MHz. This method was used in combination with signal averaging and a moveable ROI to produce an attenuation map or image.

To produce the attenuation map, a ROI of a determined size was moved throughout the

$$\alpha = \beta f$$

Equation 5

three-dimensional data space until an attenuation map was produced. The dimensions of the ROI were varied and tested. Three different ROI settings were used to test the attenuation calculation ability of the system. The first setting was a 2D ROI (Area map) where the width (x direction) of the ROI was 1 cm. This produced an attenuation calculation that was averaged over 10 a-lines. The second setting was a small 3D ROI (Vol3 map) where the width was 3 mm and the height (y direction) was 3 mm. This setting produced a calculation that was averaged over nine a-lines. The final setting was a 3D ROI (Vol5 map) that was slightly larger. The x and y dimensions of this setting were 5 mm by 5 mm. This setting produced a calculation that was averaged over 25 a-lines. At each of the settings, ROI depths (z direction) of 1.0, 1.5, 2.0, 2.5, 3.0, and 3.5 cm were tested.

Once the ROI size was selected, it was moved throughout the data space incrementally by 1.0 mm in the x and z directions. The attenuation-slope value for each calculation was assigned to a point in the center of the ROI, thus producing an attenuation map. In order to relate the results of the three settings, the ROI position was set such that the map produced from each ROI setting represented the same 2D space. Therefore, Vol5 map required two data slices on either side of the center slice, Vol3 map required one slice on either side, and Area map did not require any additional slices.

## Force Balance Comparison

In order to validate the attenuation measurements made by the attenuation mapping system, a force balance station was assembled. This station used a reflecting target, an ultrasound transducer (different from the imaging transducer), and a scale to measure the attenuation. The reflecting target was used as a transducer to convert acoustic energy into a mechanical force, which was read by the scale. Two slabs of the graphite/agar phantom tested in the attenuation mapping system were tested in the force balance. Each slab had a different thickness ( $d_1$  and  $d_2$ ). The force or weight ratio ( $w_1/w_2$ ), as read on the scale, is the same as the power ratio of the ultrasound wave as it passes through the different distance of the same material. Therefore, the weight ratio was used to compute the attenuation coefficient at the frequency of the transducer by using Equation 6. The attenuation coefficient calculated from the force balance was then used to

$$\alpha = \frac{-\ln\left(\frac{w_1}{w_2}\right)}{2(d_2 - d_1)}$$

Equation 6

calculate the attenuation coefficient at 1.0 MHz and used as a standard for the attenuation mapping system.

## Results

This study is focused on determining the accuracy and repeatability of attenuation measurements when the ROI dimensions are changed. Three sets of data were acquired and analyzed to produce an attenuation map for each ROI setting and depth. From this map, an area of interest was selected where the entire ROI for the calculations was within the phantom (there were no interfaces within the ROI). The area of interest was approximately 3 cm wide and 1 cm deep and represented approximately 300 computed values of attenuation. For each test, the attenuation coefficients within the area of interest were averaged. The mean values were then used to determine the accuracy and repeatability of the measurement system.

The results show that the accuracy of the attenuation measurement system is most dependent on the depth of the ROI (see Figure 18). For all test settings, an ROI depth greater than or equal to 2.5 cm produced accurate estimations of the attenuation coefficient for the graphite/agar phantom. However, histogram plots of the attenuation coefficient from an area of interest show that the Vol5 map setting (5mm by 5mm in the x and y directions) is the best setting for calculating an attenuation coefficient (see Figures 19–21). In addition to providing more accurate attenuation calculations, the Vol5 map setting provides improved lateral resolution within a 2D-attenuation image. Therefore, the Vol5 setting with an ROI depth of 2.5 cm is the best setting for determining the attenuation coefficient of small regions and for producing an attenuation map.

Detailed results can be found in [27].

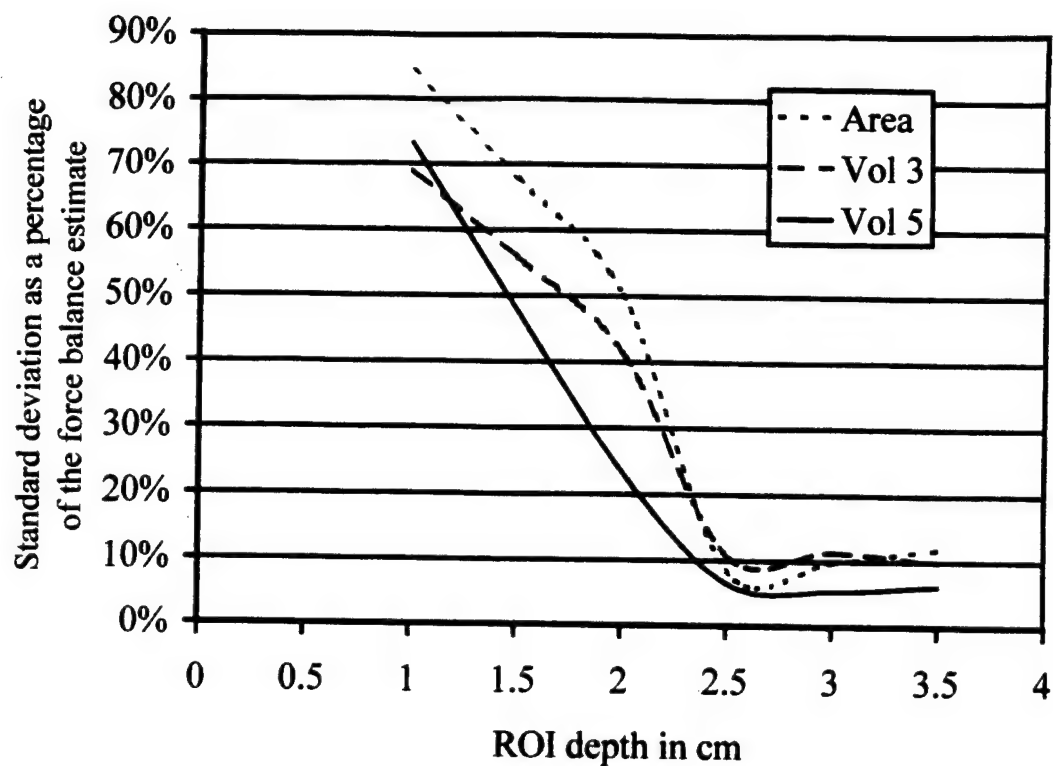


Figure 18: This shows the decrease in the standard deviation of the attenuation predictions as the ROI depth is increased.

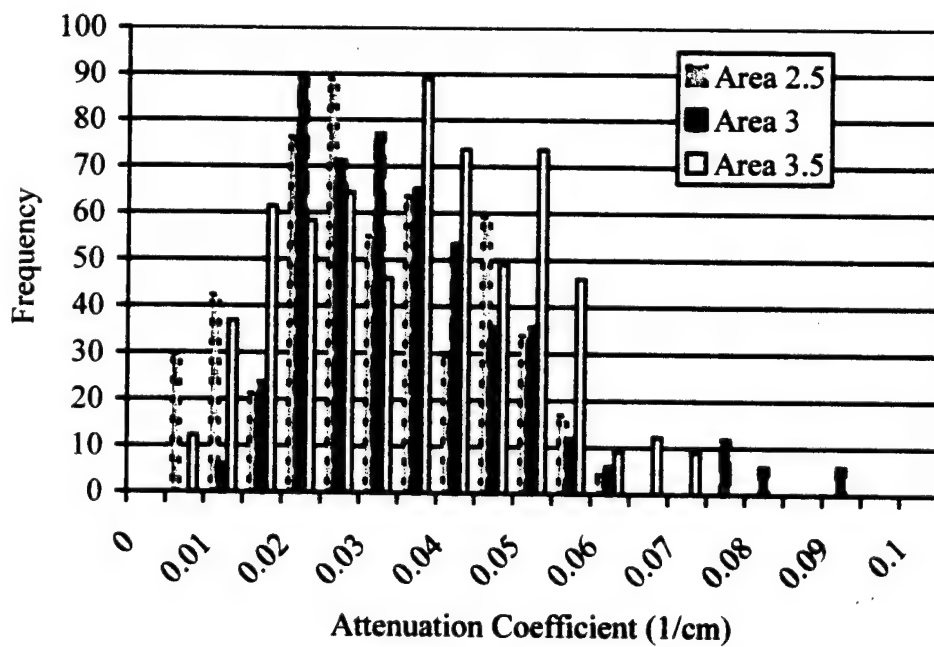
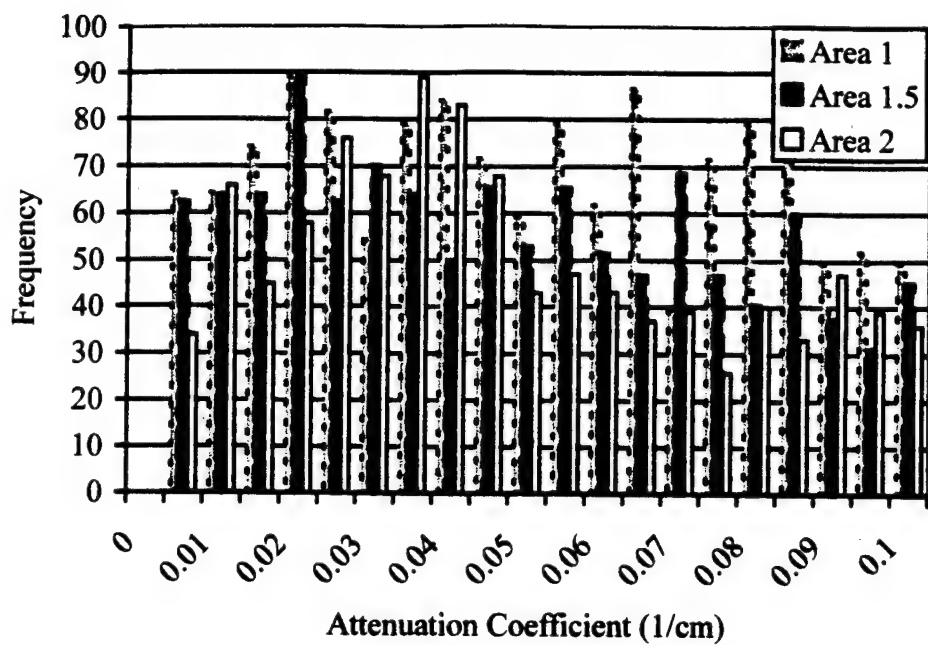


Figure 19: This shows the changing spread of the histogram of attenuation values changing as the ROI is extended in the depth direction.

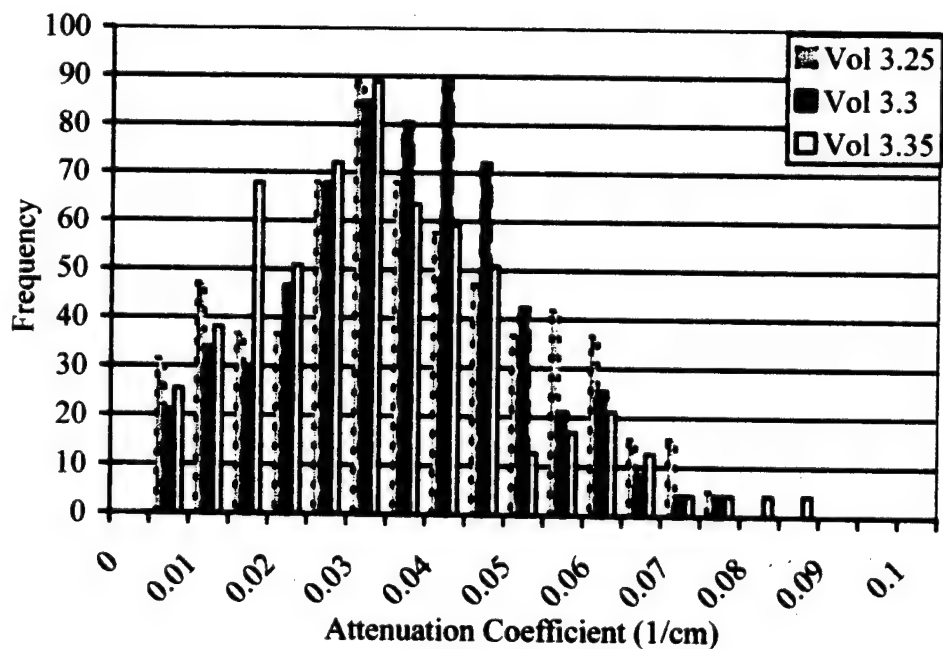
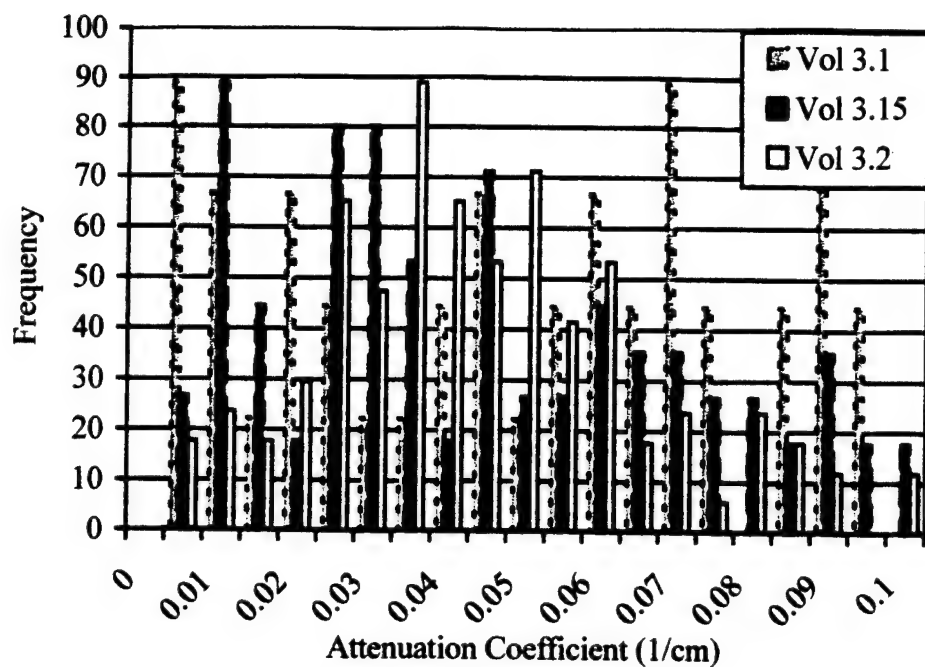


Figure 20: This shows the changing spread of the histogram of attenuation values changing as the ROI is extended in the depth direction.

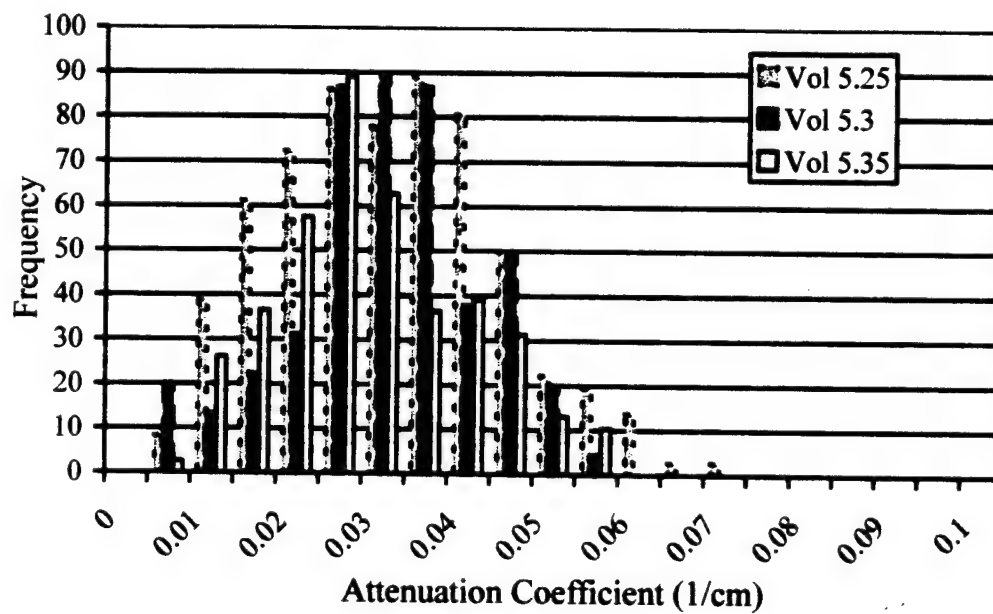
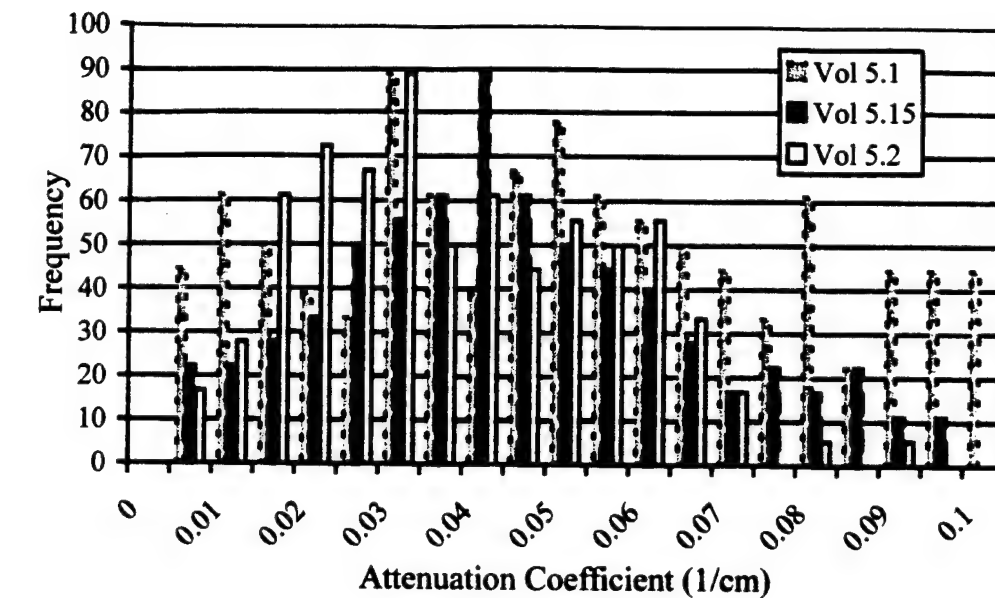


Figure 21: This shows the changing spread of the histogram of attenuation values changing as the ROI is extended in the depth direction.

- Software and hardware for clinical patient geometry acquisition completed.

During the fourth year the patient geometry acquisition system was completed. This required the completion of the Geometry Acquisition and Display Software (GADS) and completion of the patient registration system.

Figure 22 shows the clinical system and Figure 23 shows the basic hardware. An imaging transducer is mounted on the gantry that moves the treatment transducer, and the two transducers are moved together.

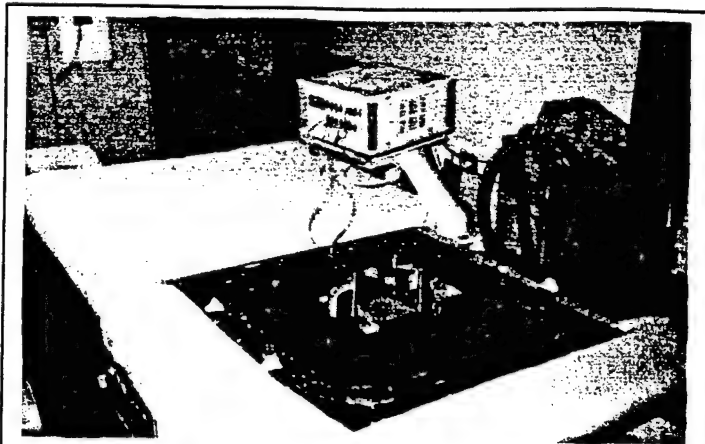


Figure 22: Clinical Hyperthermia System.

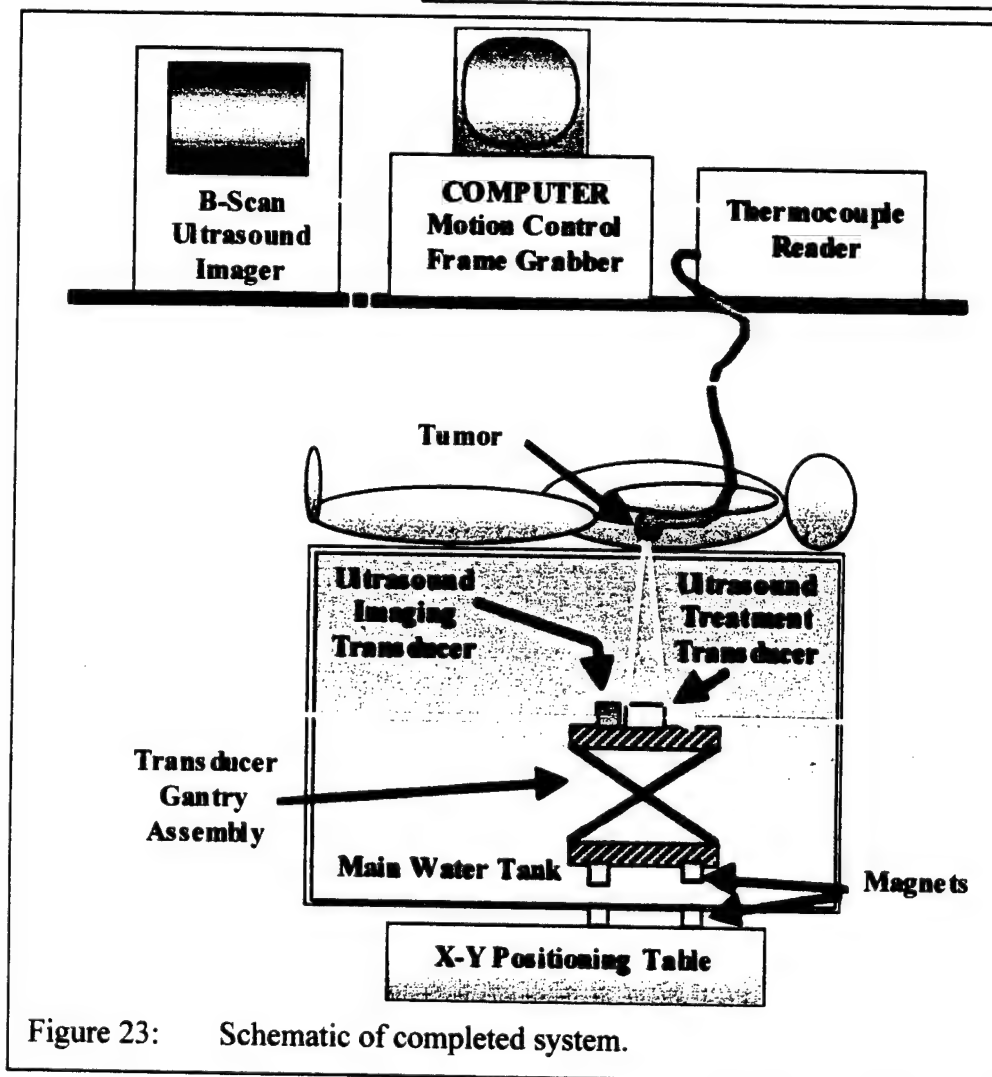


Figure 23: Schematic of completed system.



As the motion controller moves the transducer the B-scan imager produces images that are captured by the Frame Grabber.

At this point the GADS software takes over. Image sets are recorded and organized along with pertinent patient data. In GADS, the images are automatically composited using the known x, y, z information from the motion controller. In this example, the transducer has been translated to three positions that lie side by side, in the plane of the B-scan image. The detailed operation of the system has been described previously. The following extended Figure (Fig. 24) includes a series of screen captures that will clarify the operation of the software.

**Patient Information**

File

Last Name:

First Name:

Social Security Number:  -  -

**Image Collection Information**

Transducer Width (mm):

Number of Scans Wide:

Frequency (MHz):

Node Size (mm):

X Start Position (mm):

Y Start Position (mm):

X End Position (mm):

Y End Position (mm):

Z Position (mm):

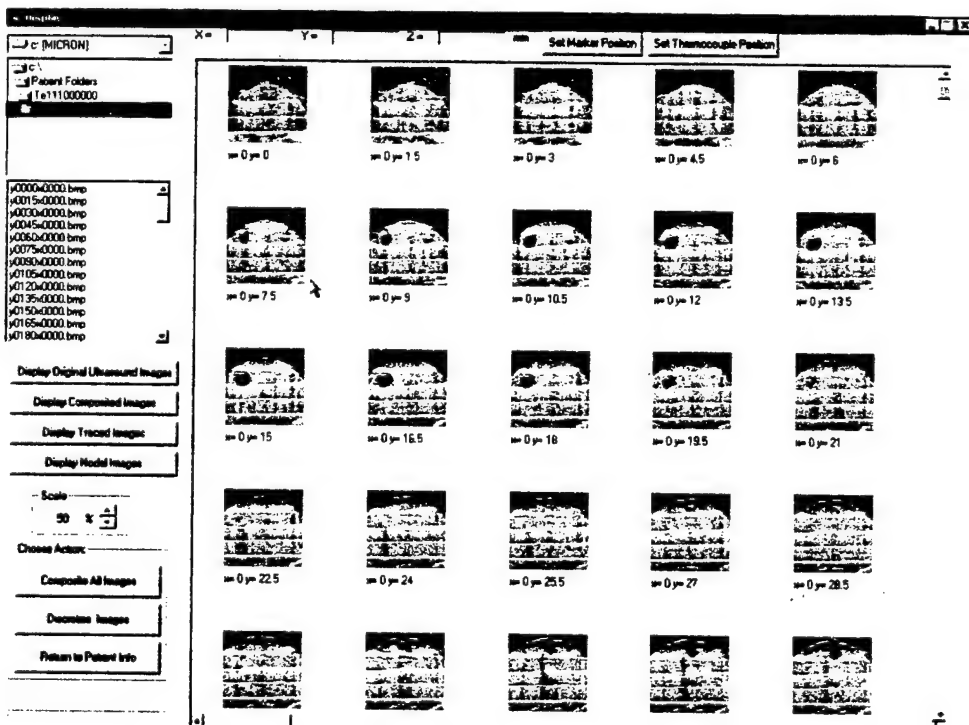
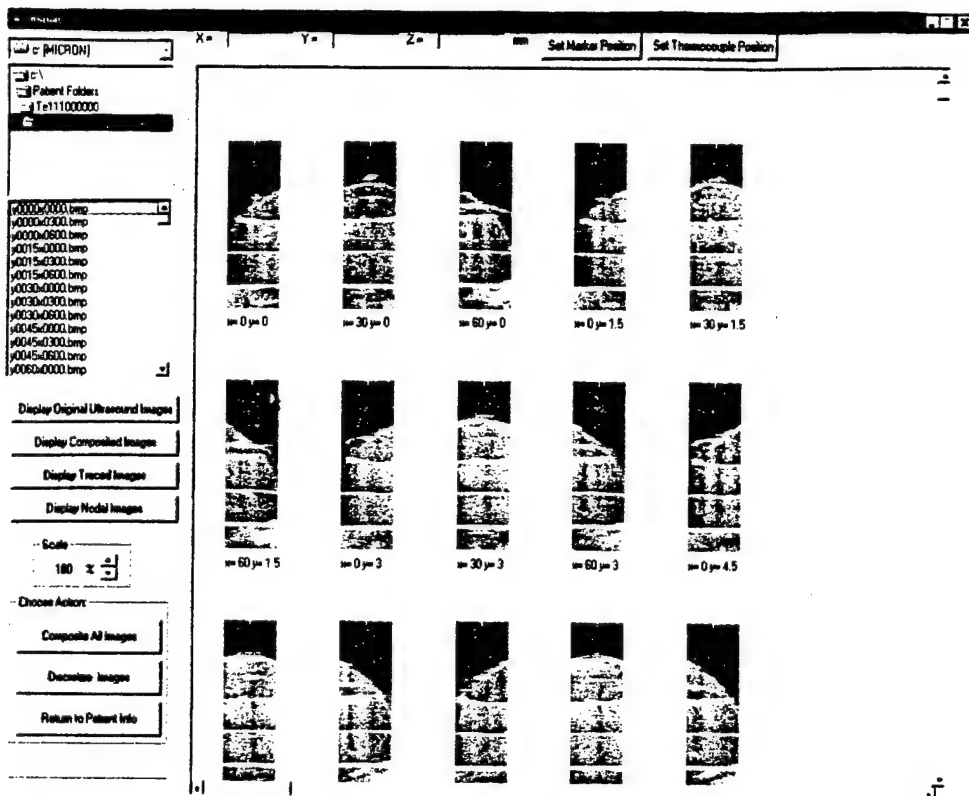
Description:

Date Created (mm/dd/yy):

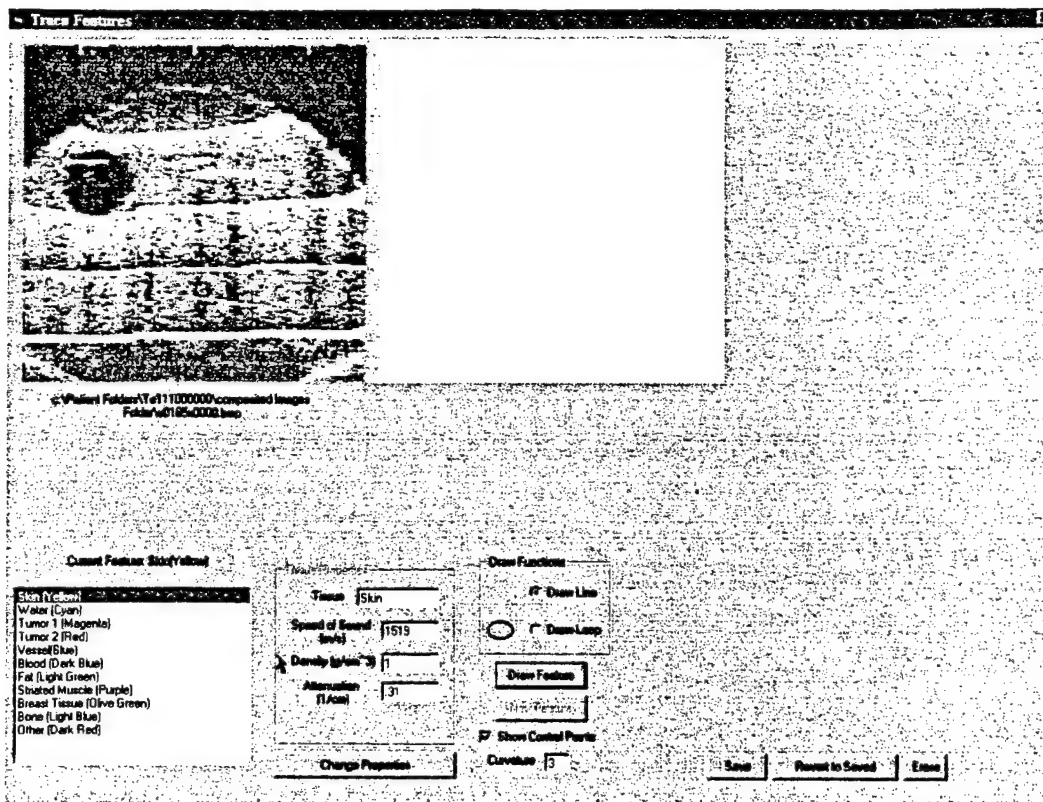
Doctor(s):

Technician(s):

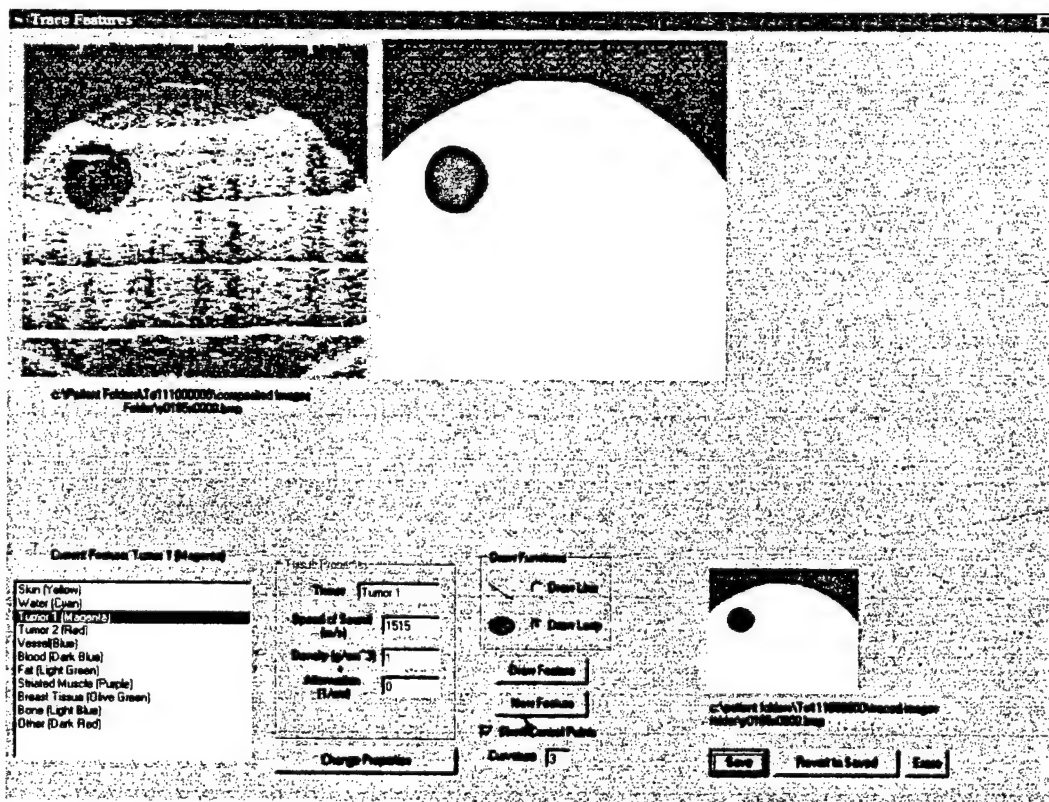
Patient Information Window.



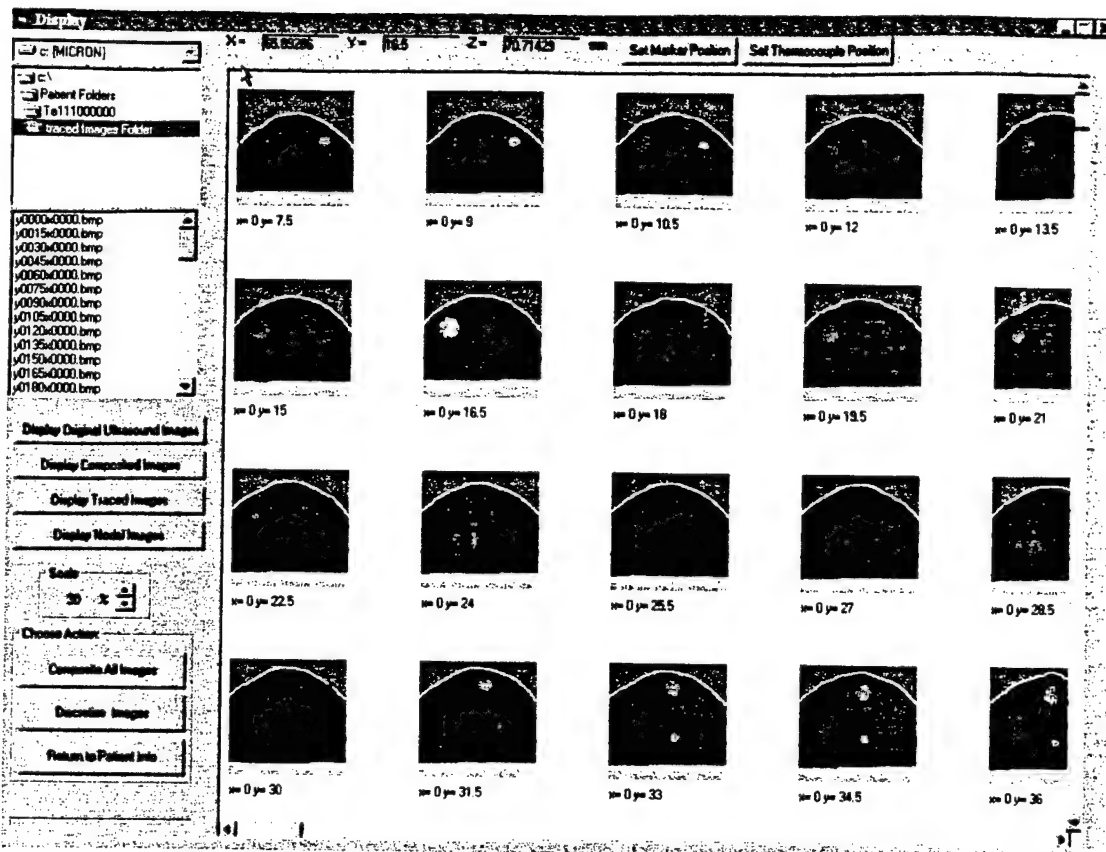
This shows the B-scan images before and after they have been composited.



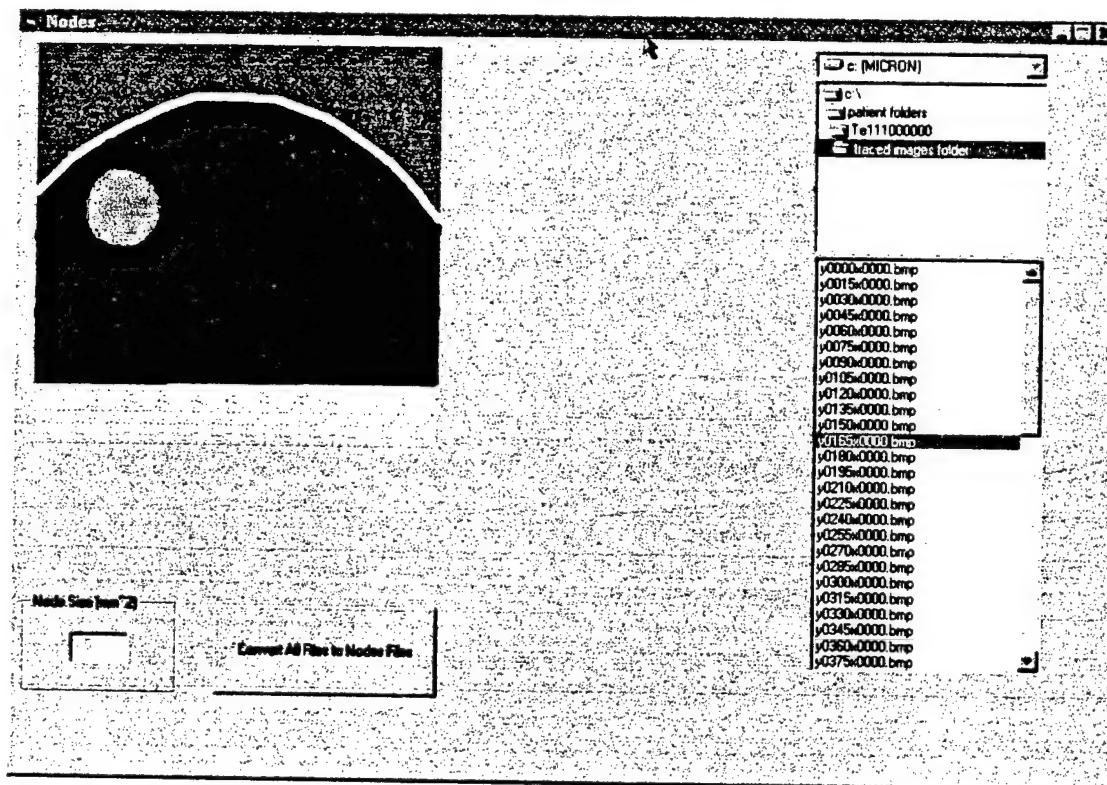
Each significant surface is manually digitized by a technician.



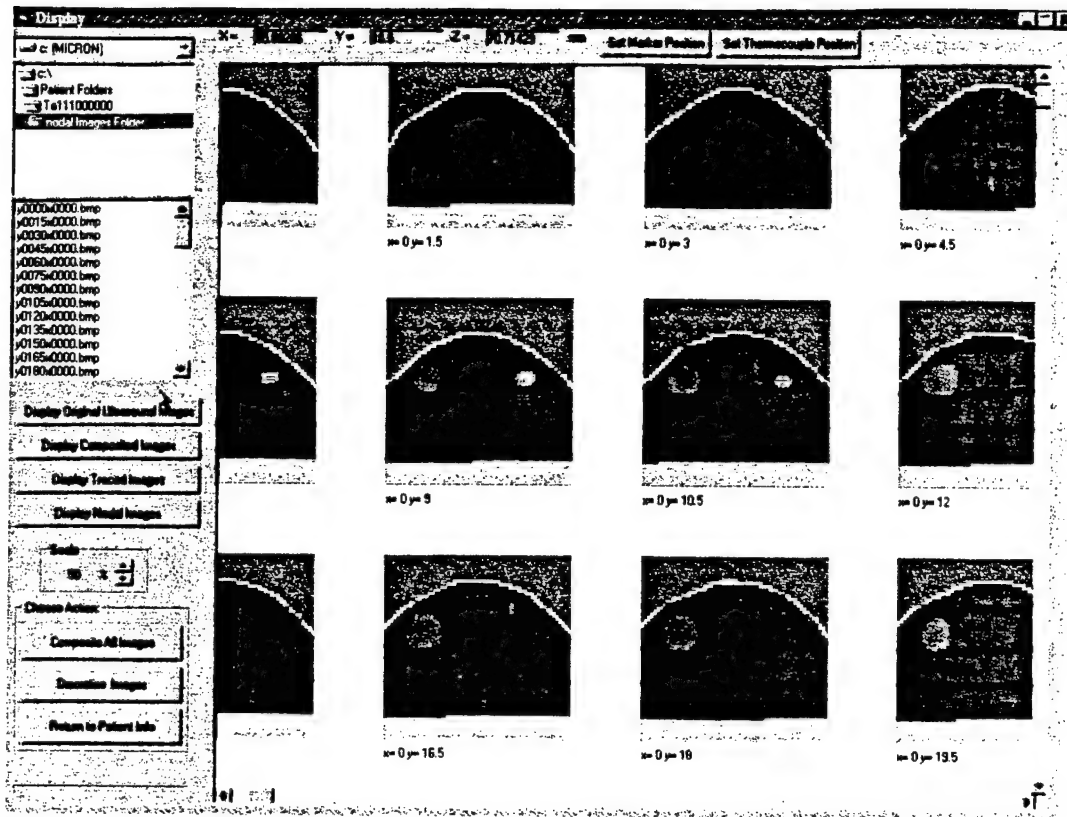
These surfaces separate the image into regions. Each region is assigned a tissue type, which assigns model parameters: density, speed of sound, and attenuation.



Once all the images have been converted...



The node size appropriate to the model is selected and the nodal values are assigned.



The results are displayed visually showing the effects of the node size.

H TestVAL Notepad				
File	Edit	Search	Help	
68	62	59		
Other	1	1	1500	0
Breast Tissue	3	1	1510	.22
Blood	4	1.84	1566	0.813
Muscle	5	1.84	1552	.130
Water	6	1	1500	0
Tumor2	249	1	1500	0
Fat	250	0.92	1478	.07
Skin	251	1	1519	.31
Vessel	252	1.80	1530	.19
Tumor1	253	1	1515	0
Bone	254	1.82	3445	1.6

The various tissue types and their assigned properties are recorded in a table.

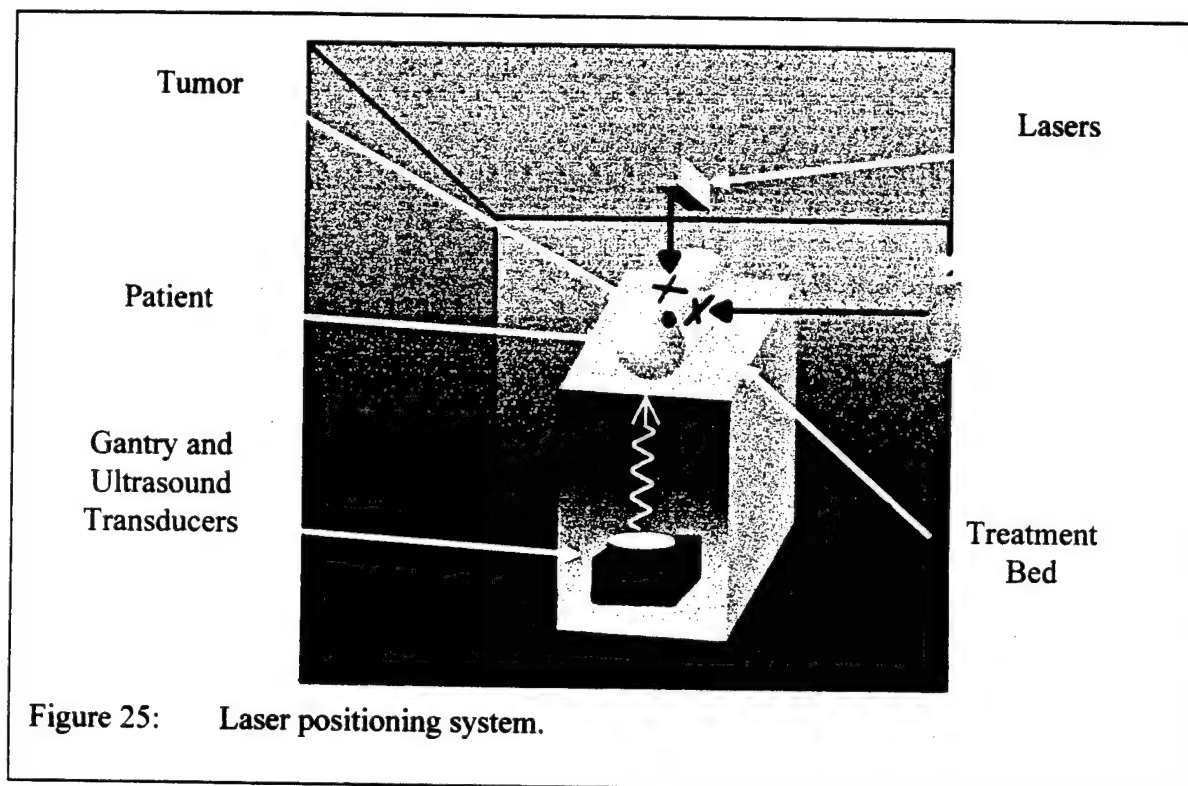
Figure 24: Operation of the Geometry Acquisition and Display Software (GADS).

## Patient Registration

The final system developed to reliably and repeatably position the patient for treatment uses three systems:

1. Laser Alignment
2. Thermoplastic Immobilization
3. Ultrasonic Markers

The laser alignment system uses tattoos on the patient's skin that are aligned to lasers permanently positioned above and to the side of the treatment table (see Figure 25). Once positioned using the laser system, the patient is locked into place using a thermoplastic sheet. This sheet is molded to the patient's body during the first visit and helps return the patient to an identical position on subsequent visits (see Figure 26). 1/4 inch diameter disks of this steel shim material, acting as ultrasonic markers, are placed on the patient's skin near the treatment region and are used to verify the location of soft tissue in the treatment region. Figure 27 shows the appearance of the markers in a B-scan image.



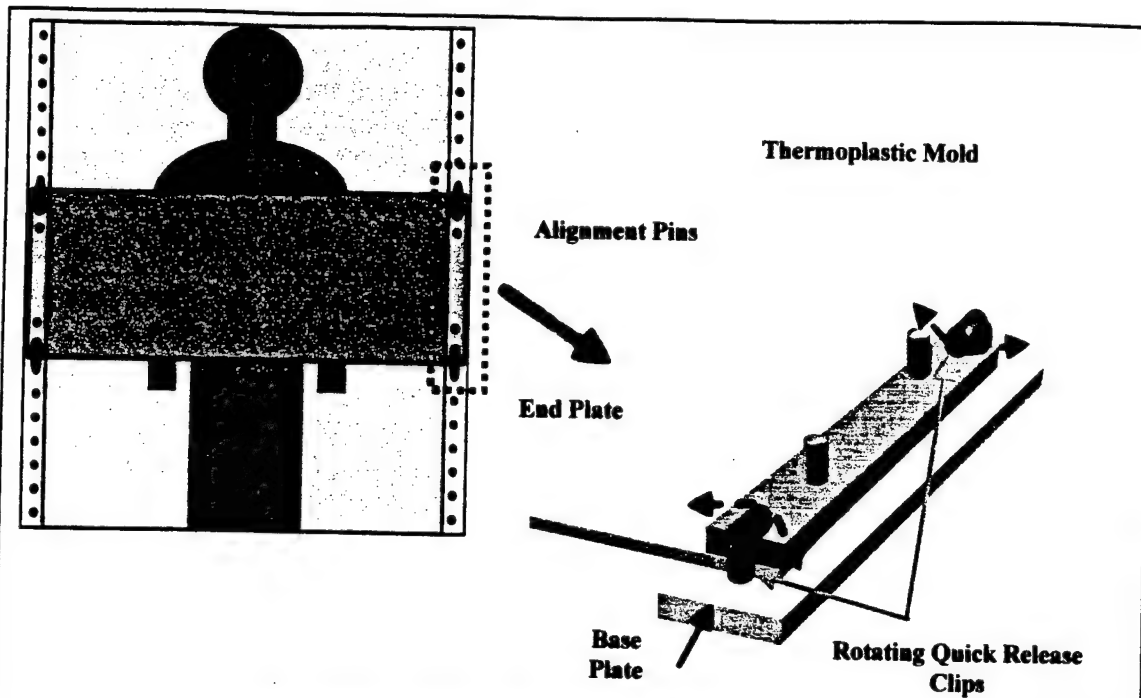


Figure 26: This shows the design schematic for the Thermoplastic Positioning System along with the completed system.



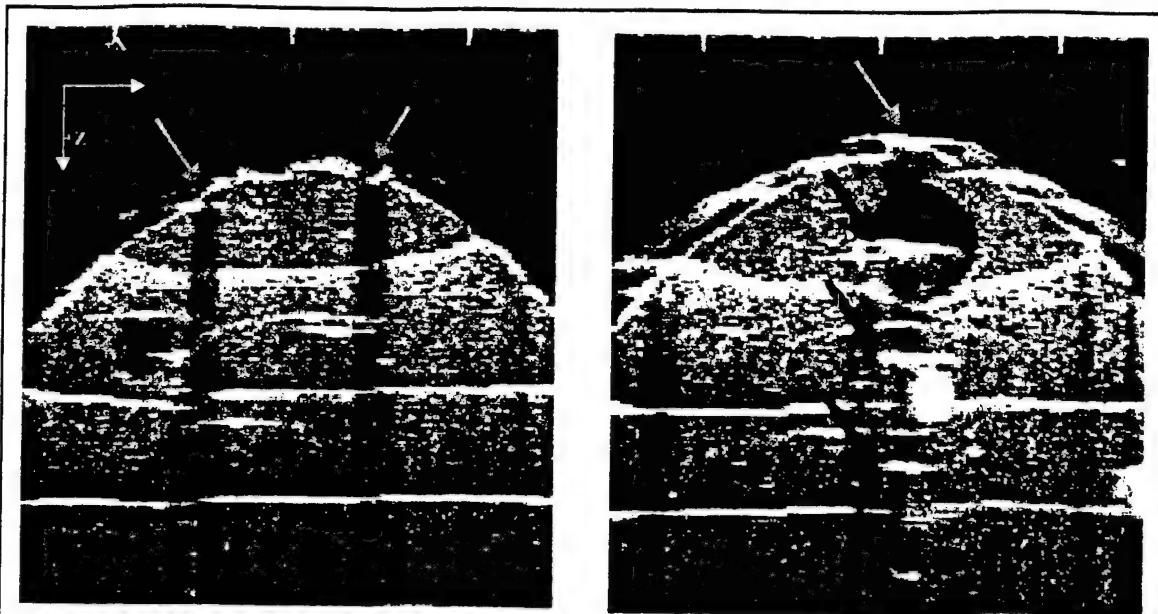


Figure 27: This shows the appearance of the ultrasound markers in a B-scan image. There are two possible artifacts associated with these markers. On the left, the markers create shadows where little ultrasound energy passes through the marker to tissue below. On the right, the marker happens to be normal to the transducer face and multiple reflections from the marker are seen.

- **Verification tests completed**

The following experiment was performed in order to estimate the accuracy and repeatability of the ultrasound geometry acquisition system.

### **Experimental Setup**

Nine five-millimeter diameter ultrasound-reflecting markers were punched out of a sheet of 0.003-inch thick steel shim using a circular paper hole-punch. The circular markers were adhered to a Gammex<sup>TM</sup> RMI-429 Ultrasound Biopsy Phantom using a thin coat of contact cement. The relative positions of the center of each marker were measured with respect to the central marker (Marker 4) using the three-axis positioning system of a milling machine. The phantom was fixed to the milling machine table so that the markers were on the superior side and a pointed mill bit was visually aligned with the center of each marker. Figure 28a shows a schematic top view of the markers' relative positions on the biopsy phantom and Figure 28b plots the measured marker positions using Marker 4 as the origin of the coordinate system. Figure 29 is a general schematic of the phantom installed in the test apparatus.

The central marker (Marker 4) lay on an approximately horizontal surface at the peak of the phantom. Due to the dome shape of the biopsy phantom, the four markers closest to this central marker (Markers 2, 3, 5, and 6) were angled approximately 30 degrees off the horizontal

plane. Similarly, the markers furthest from the center (Markers 1, 7, 8, and 9) were tilted approximately 45 degrees off the horizontal plane.

## Results

The results showed that reflectors could be used to detect patient movements with an accuracy of approximately 1.5 millimeters. The repeatability found between three tests was exceptional, with the error calculated to be less than approximately one millimeter.

Results from this experiment suggest that an averaging algorithm that would automatically calculate the central location of a series of points selected on a particular marker could substantially improve the accuracy and efficiency of the technique. The information could also be used to translate the treatment plan coordinates to the new patient position, saving operators valuable time that would otherwise be spent repositioning the patient. A similar system could also be used to aid in locating thermocouple catheters prior to treatments in order to expedite the process of finding thermocouple junctions and to help reduce pain often associated with this search. More detailed information is available in [28].

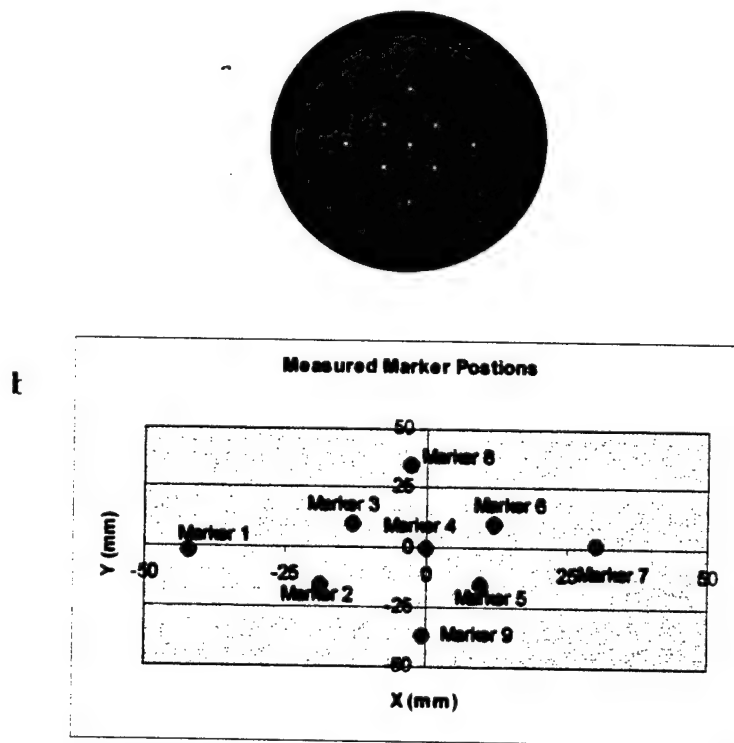


Figure 28: a.) Top view of ultrasound-reflecting markers on the surface of the biopsy phantom. b.) Measured marker positions with respect to Marker 4.

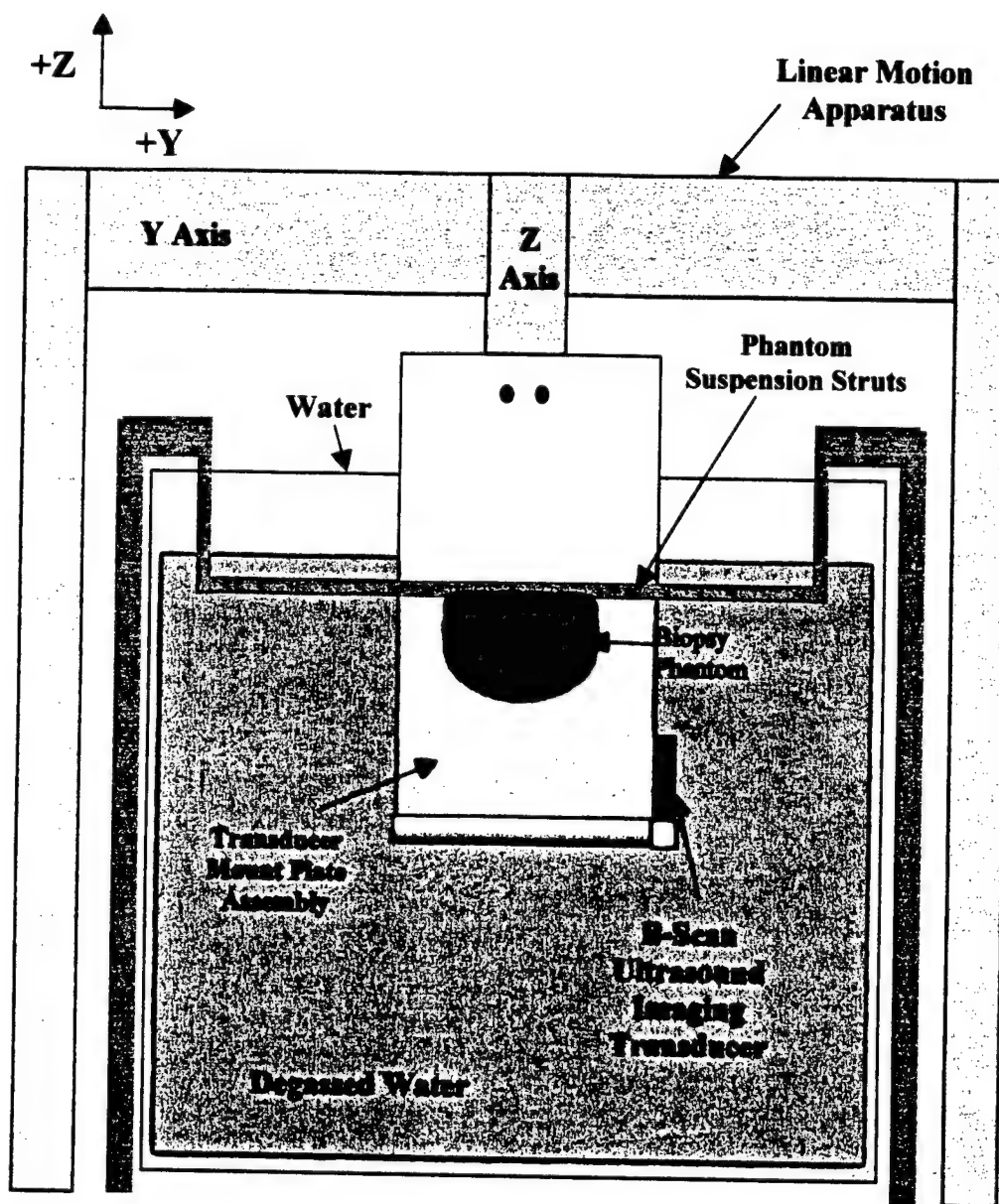


Figure 29: Schematic of linear motion apparatus, phantom, and ultrasound transducer in the water tank.

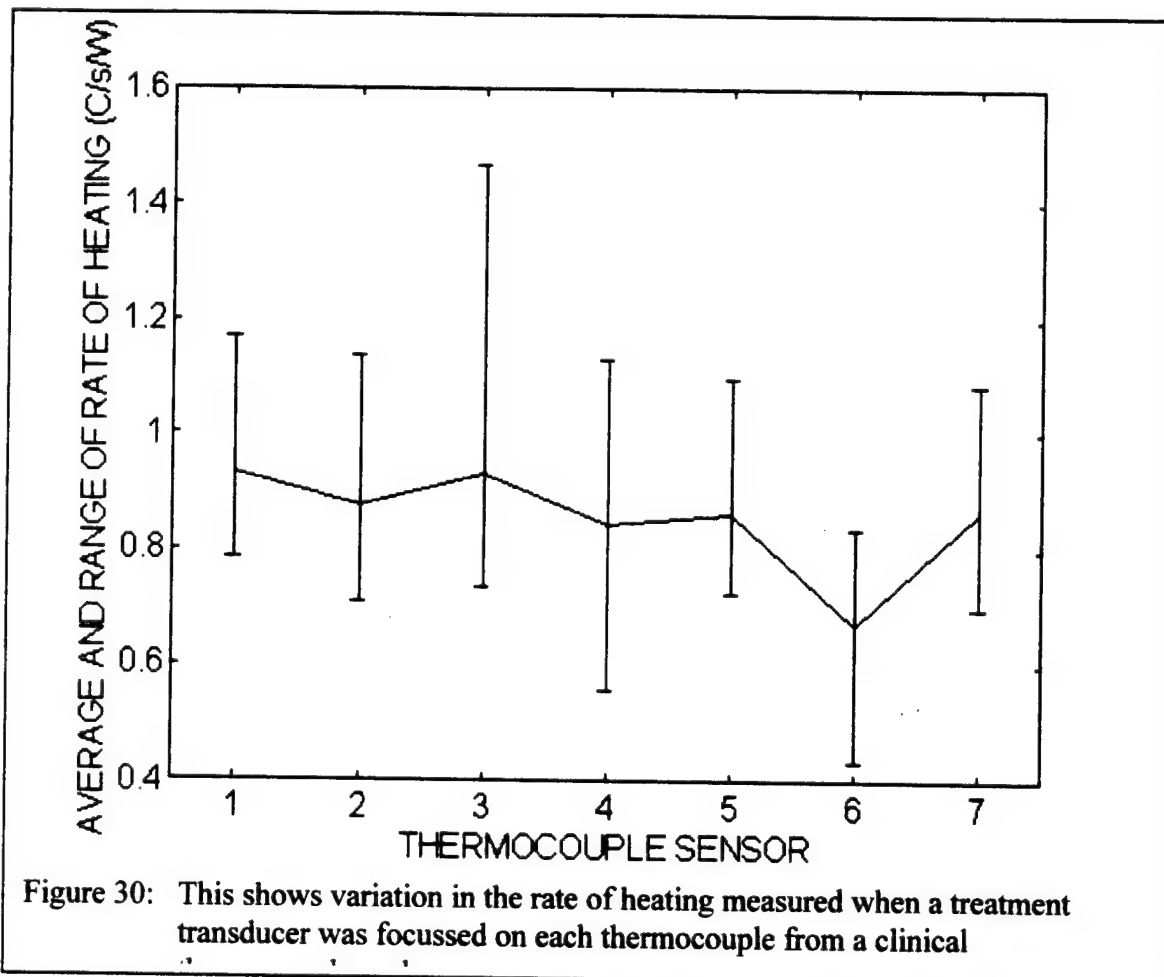
## **Subsystem 2: Experimental SAR Measurement**

- **Probe orientation effects on the SAR measurements were investigated experimentally.**

A re-examination of experimental results from Year 3 and a series of new tests using agar phantoms showed unexplained variations in the thermocouple based SAR measurements. Continued experiments in Year 4 document and explain these variations. A new thermocouple probe was designed to minimize these variations.

Figure 30 is the result of an experiment where a clinical thermocouple probe, described below, was immersed in a water bath and each of the seven thermocouple junctions was in turn heated by placing it in the focus of an ultrasonic treatment transducer and turning the transducer on briefly. While the ultrasound power and relative positioning between thermocouple and transducer were held constant, the rate of heating measurement varied dramatically from thermocouple to thermocouple and from measurement to measurement when repeating experiments on the same thermocouple.

In order to explain this variation (and perhaps eliminate it) a series of experiments were performed where the angle of ultrasound incidence on the probe was varies as well as the axial orientation of the probe (i.e. the probe was rotated about it's axis). This experiment and results are described below.



## LABORATORY TESTING APPARATUS

### Ultrasound Power Field Generation

A diagram of the laboratory testing apparatus can be seen in Figure 31. The input power signal was generated by a function generator and amplified by an rf amplifier. After amplification the power signal was routed through a power pick off box with attached power meter to measure forward and reverse electrical power. The power signal continued out of the power pick off box, passed through an impedance matching box and terminated at the ultrasound transducer. Any one of several different custom-built ultrasound transducers can be chosen to deliver an intensity field in the test tank. Table 2 is a list of the transducers available for use.

**Table 2: Available Ultrasound Transducers.**

Shape	Diameter or Width (cm)	Focal Length (cm)	Frequency (MHz)
square	4	$\infty$	1.5
square	4	$\infty$	1.0
circular	3	$\infty$	3.93
circular	7	25	0.5
circular	10	20	2.0
circular	10	20	1.5

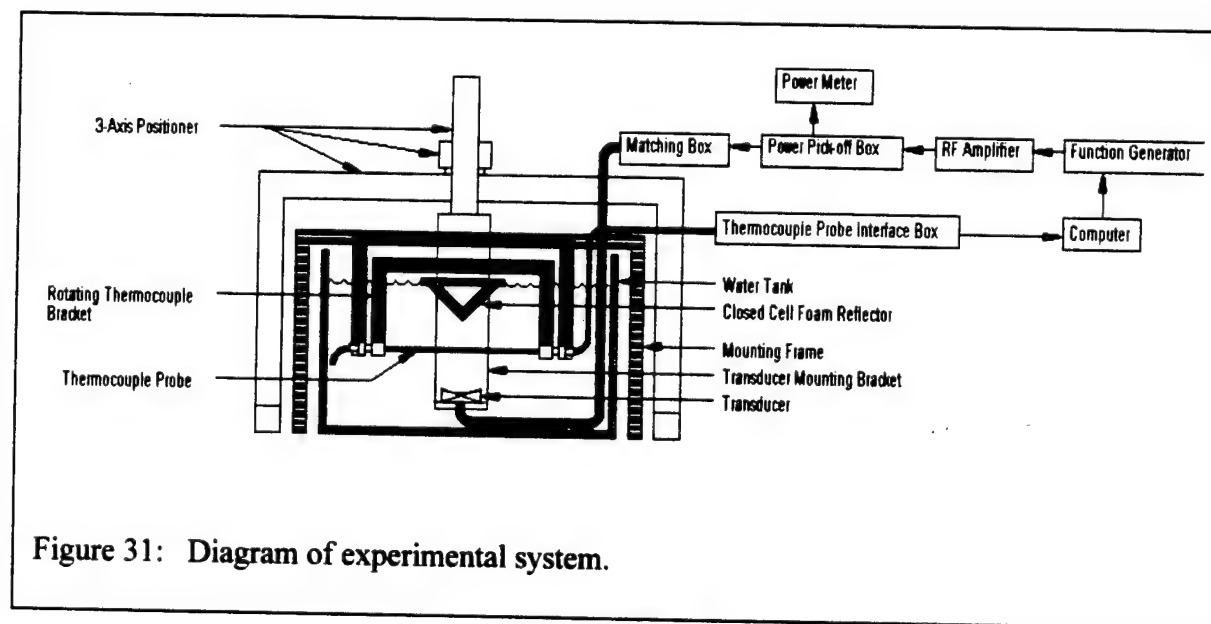


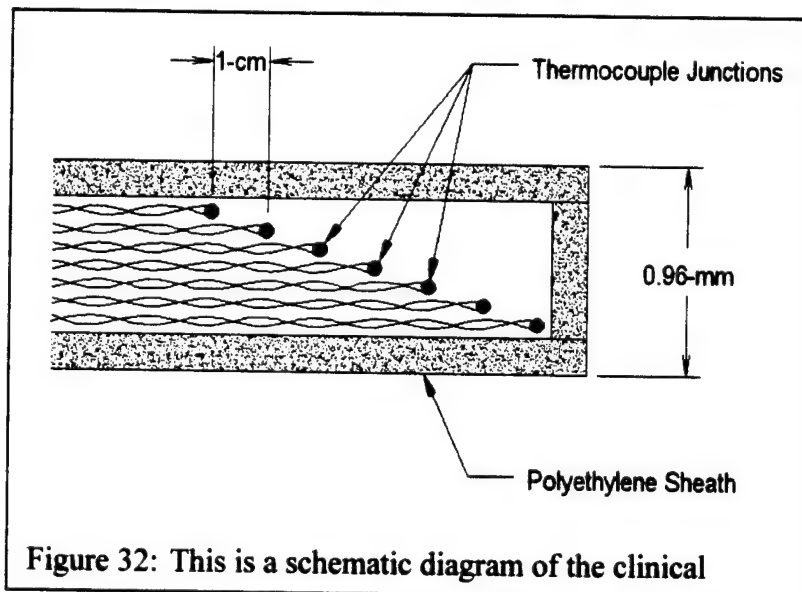
**Figure 31: Diagram of experimental system.**

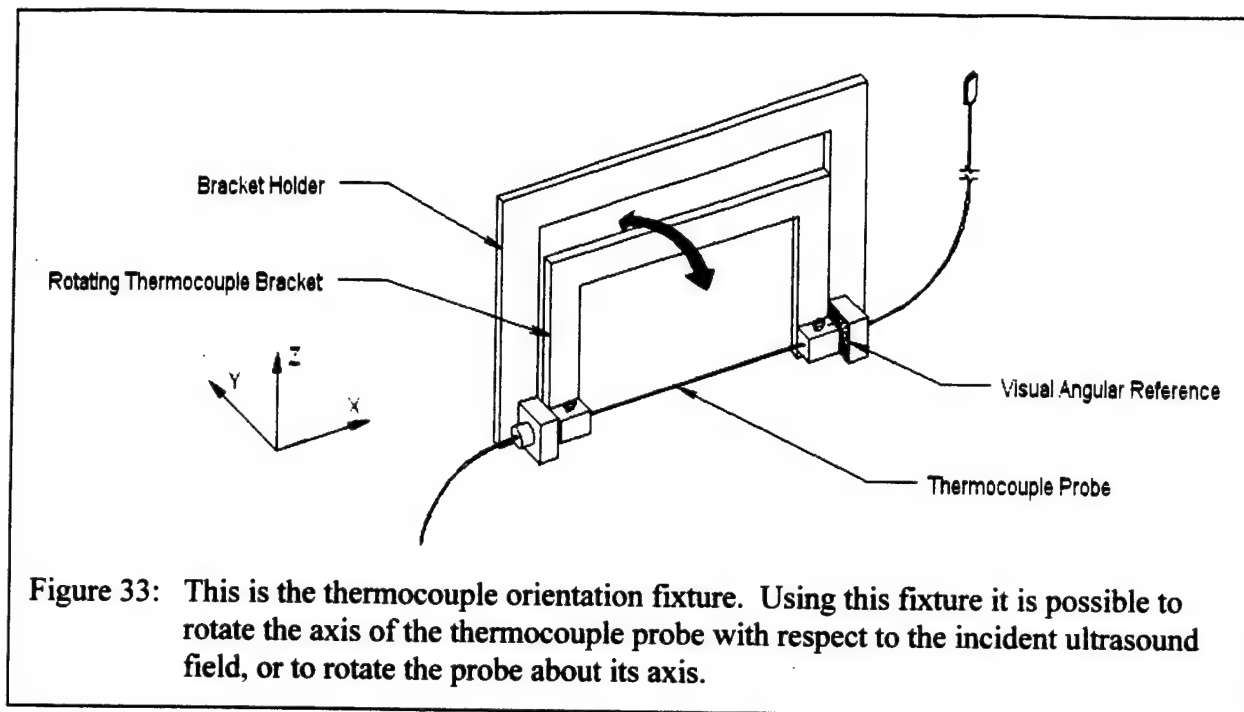
## Temperature Measurement

Thermocouple output was measured by a computer connected to a custom-built thermocouple interface box. The thermocouple interface box can rapidly sample as many as 16, 7-junction thermocouple probes. The thermocouple probe, which was described by Anhault and Hynynen, 1992, and illustrated in Figure 32, consists of seven Manganin Constantan thermocouple junctions spaced at one centimeter intervals and encapsulated in an air filled polyethylene sheath (o.d. 0.96-mm and i.d. 0.58-mm). The thermocouple junctions were manufactured by soldering together a 50- $\mu$ m Manganin wire and 50- $\mu$ m Constantan wire. The diameter of the soldered sensor varies but is approximately 0.3-mm in diameter. A variable temperature isothermal water bath was used to calibrate each probe using a two-point calibration technique. Calibration data for each thermocouple was stored in the computer and used during temperature measurement.

## Mounting and Positioning System

The three-axis positioning system shown in Figure 29 was placed adjacent to the water tank so that the positioning arm overhung the tank. The L-shaped transducer mounting bracket was attached to the positioning arm and extended towards and across the bottom of the tank. The transducer was fixed to the transducer mounting bracket and leveled so that the ultrasound field was generated towards the surface of the water. The tank was filled with degassed water with oxygen content of less than 2-ppm. During early ultrasound experiments bristle brushes were used to absorb and disperse the ultrasound, however it was apparent from test results that some reflection was returning from the surface back to the test specimen. A reflecting target made of closed cell foam was substituted for the bristle brushes and towels were draped around the inside of the water tank to completely direct and absorb the excessive ultrasound intensity away from the test specimen. Platforms for holding phantoms and brackets for holding thermocouples in the energy field were fixed to a steel frame that encased the water tank. Several different apparatus were used during various tests to hold and position the test specimens, but the fixture below was used in the experiments described here.

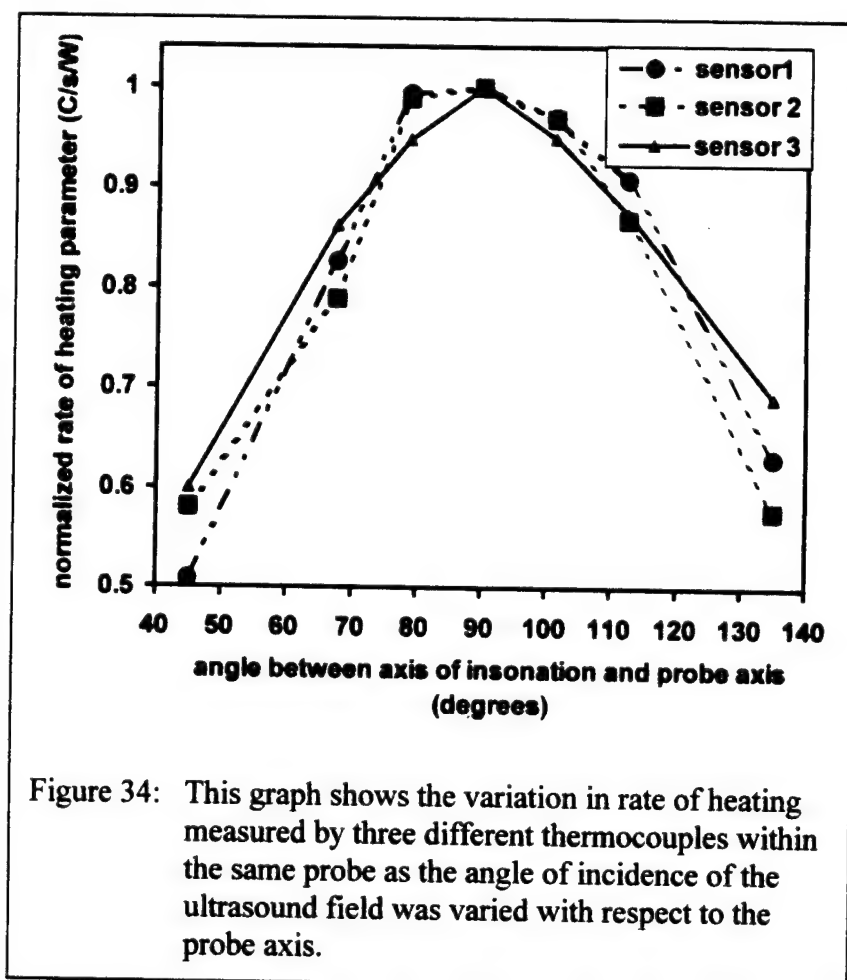




## Results

When the axis of the probe was rotated with respect to the incident power field, the result shown in Figure 34 was produced. This figure represents three trials as the probe was rotated to a position, then heated, then rotated again. While there is some scatter between repetitions, it is clear that the measured power drops by over 30% once the angle of incidence reaches 30° away from normal incidence. While this variation is significant, if the probe orientation is known, the variation could be corrected mathematically.

In a second experiment, the thermocouple probe was placed in the ultrasound field at normal incidence (with the probe axis at 90° to the wave propagation vector.) Each thermocouple was placed in the

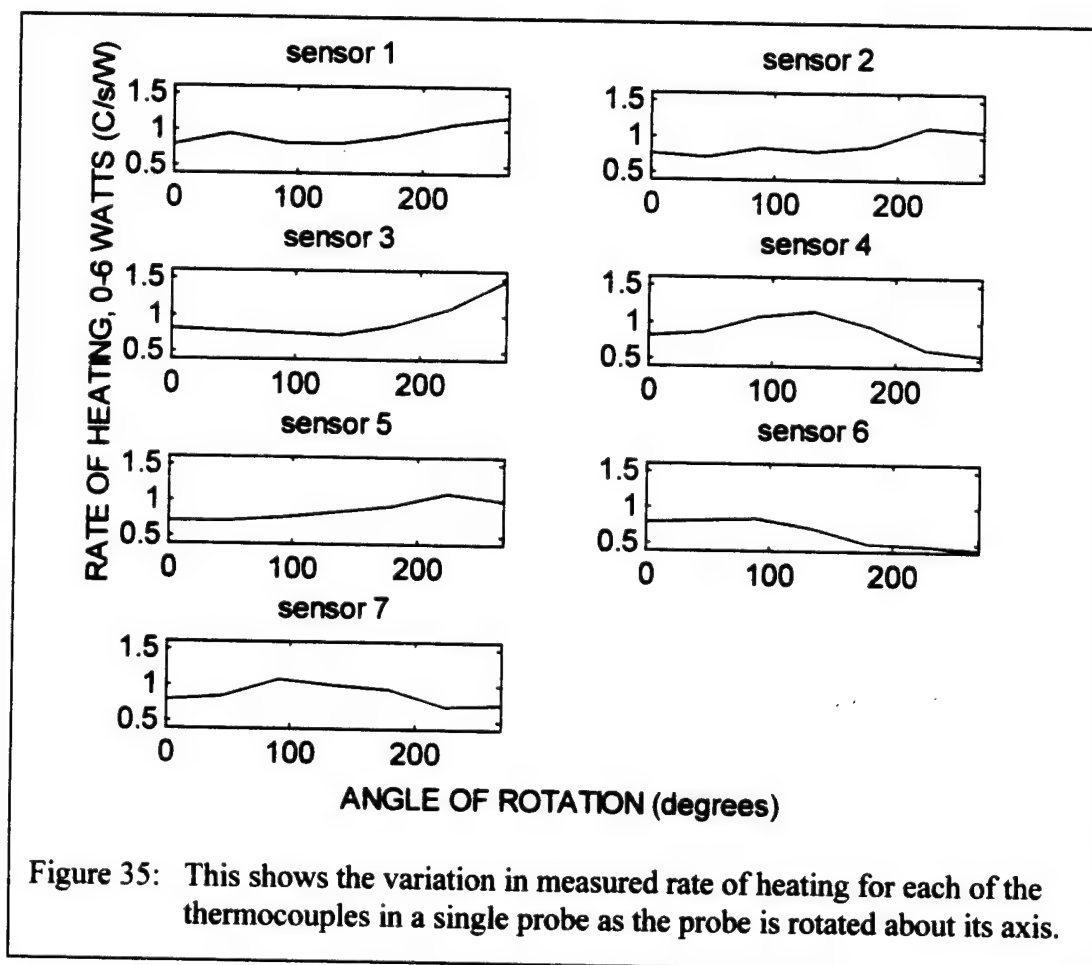




focus of the ultrasound transducer and then heated. After heating, the probe was rotated about its axis and the experiment was repeated. This was performed for each of the seven thermocouples in the probe. The results of this experiment are shown in Figure 35. Note that there are significant variations with angle of rotation and from thermocouple to thermocouple. This behavior is attributed to a semi-random placement of the 0.3mm thermocouple junction within the 0.58mm inside diameter of the tube. In order to better understand this behavior, the finite difference model developed previously was used to analyze the system.

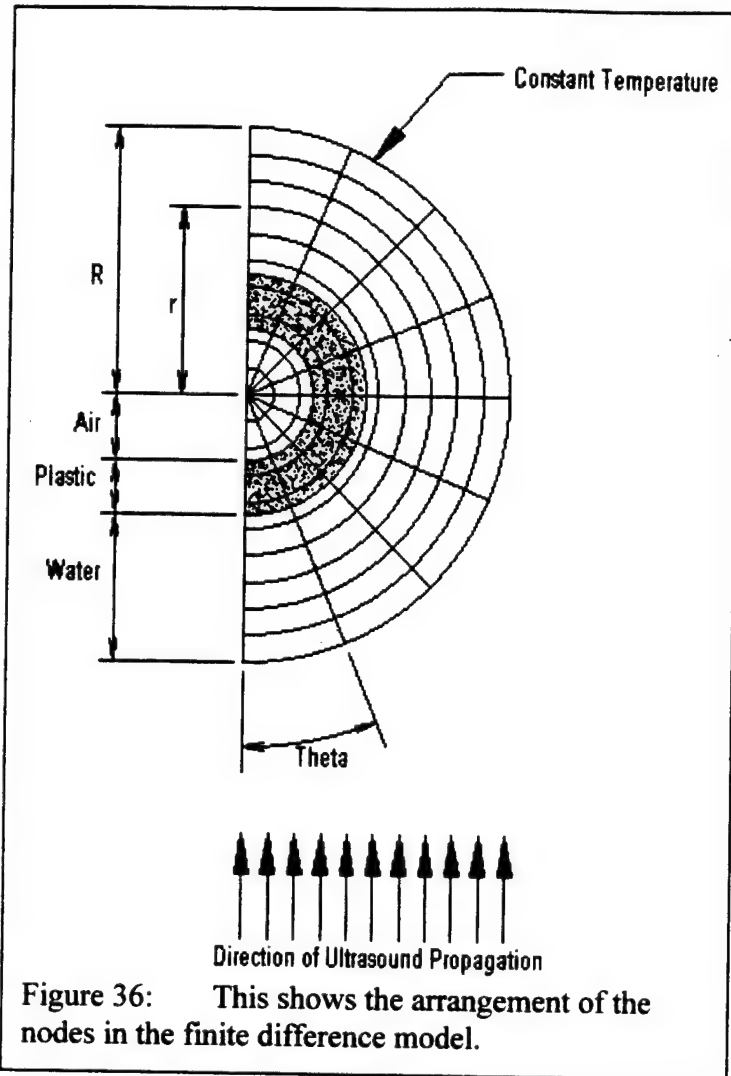
### Finite Difference Model

A finite difference model of the plastic sheathed thermocouple probe was created using the forward difference technique and the Matlab® software package. The model geometry represents a thermocouple probe placed on the axis of insolation of a power density field generated by a hyperthermia treatment transducer. The finite difference model was created to simulate the transient response of the thermocouple probe at the onset of insolation. Figure 36 illustrates the 2-D cylindrical coordinate system used to model a cross section of the probe in a water bath. Due to symmetry of probe and incident ultrasound only half of the total cross section needed to be modeled. The program allowed for variation of the model radius as well as the



number of nodes in the radial direction. The number of angular divisions could also be varied to efficiently produce meaningful results.

Use of a 2-D model instead of a 3-D model was justified because the wide energy field of the modeled treatment transducer produces a radial intensity gradient near the axis of insonation that is not steep. The smooth and nearly constant intensity profile proximal to the cross section of interest, which is centered on the axis of insonation, and the low heat conduction coefficient of the plastic produce a smooth and nearly constant temperature profile along the axis of the probe proximal to the cross section of interest. This smooth and nearly constant temperature profile along the axis of the probe near the cross section of interest does not generate extensive heat conduction down the probe relative to the heat produced by the ultrasound at the cross section of interest. The nearly constant intensity within a few millimeters of the axis of insonation also justifies the use of a constant incident intensity in the model.



The general two-dimensional cylindrical heat-conduction equation is

$$\frac{\partial^2 T}{\partial r^2} + \frac{1}{r} \frac{\partial^2 T}{\partial r} + \frac{1}{r^2} \frac{\partial^2 T}{\partial \theta^2} + \frac{\dot{q}}{k} = \frac{1}{\alpha} \frac{\partial T}{\partial t}$$

Equation 7

The heat generation in the plastic is due to the absorption of ultrasound or

$$\dot{q} = \alpha_{US} I_{pl}$$

Equation 8

where  $\alpha_{US}$  is the absorption coefficient of the plastic sheathing material and  $I_{pl}$  is the intensity of ultrasound in the plastic. However, there is an impedance mismatch between the plastic and water and the direction of ultrasound propagation is not perpendicular to the surface of the plastic, excluding where  $\theta=0$ . Losses of ultrasound intensity at the water plastic interface were accounted for using the angularly dependent reflection coefficient [Auld] and Equation 8 becomes

$$\dot{q} = \left\{ \frac{Z_2 / \cos(\sin^{-1}(\sin(\theta) \cdot c_2 / c_1)) - Z_1 / \cos(\theta)}{Z_2 / \cos(\sin^{-1}(\sin(\theta) \cdot c_2 / c_1)) + Z_1 / \cos(\theta)} \right\} \cdot \alpha_{US} I$$

Equation 9

where  $Z_2$  and  $c_2$  are the impedance and speed of sound in plastic respectively,  $Z_1$  and  $c_1$  are the impedance and speed of sound in water and  $I$  is the temporal average intensity of the ultrasound incident to the probe. Intensity loss due to attenuation in the plastic as the ultrasound propagated were not accounted for because of the small distance actually traveled within the plastic and the inherent estimation of intensity in the plastic. Estimation of the impedance of the plastic and of the effect of total reflection of ultrasound intensity at the plastic-air interface resulted in uncertainty of the actual intensity field in the plastic.

The nodal forward difference representation of the general 2-D cylindrical heat-conduction equation with the described ultrasonic absorption is

$$T_{\theta,r}^{p+1} = T_{\theta,r}^p \left[ 1 - 2\alpha_{\theta,r} \Delta t \left( \frac{1}{\Delta r^2} + \frac{1}{r^2 \Delta \theta^2} \right) \right] + \alpha_{\theta,r} \Delta t \left[ \left( \frac{T_{\theta,r+1}^p + T_{\theta,r-1}^p}{\Delta r^2} \right) + \left( \frac{T_{\theta,r+1}^p - T_{\theta,r-1}^p}{2r \Delta r} \right) + \left( \frac{T_{\theta+1,r}^p + T_{\theta-1,r}^p}{r^2 \Delta \theta^2} \right) + \frac{\dot{q}_{\theta,r}^p}{k_{\theta,r}} \right]$$

Equation 10

where each node carries its own value for  $\alpha$ , rate of  $q$ , and  $k$ .

To determine an appropriate time step for the model the value of  $\Delta t$  was determined after setting the following quantity to zero:

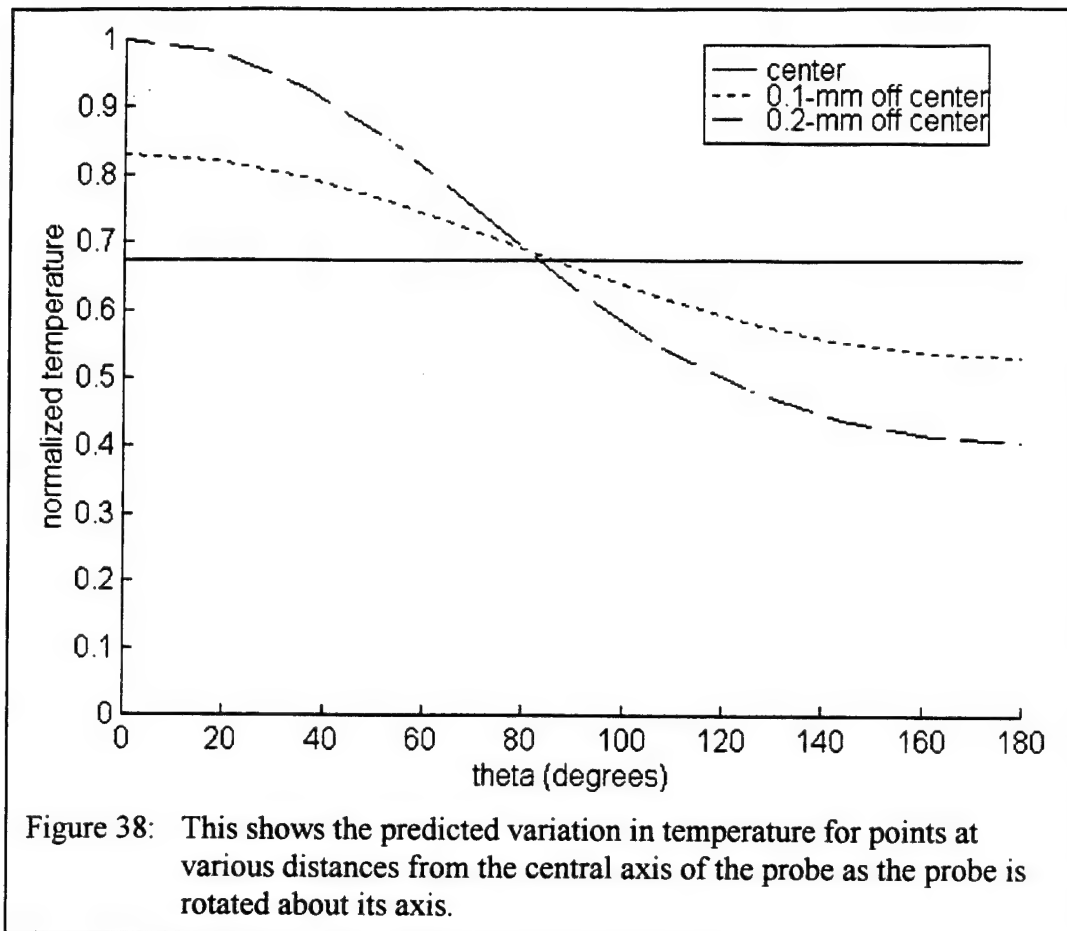
$$\left[ 1 - 2\alpha_{\theta,r} \Delta t \left( \frac{1}{\Delta r^2} + \frac{1}{r^2 \Delta \theta^2} \right) \right]$$

Equation

This value of  $\Delta t$  was the largest time step allowed which did not result in an unstable model. To avoid the problem of dividing by zero the temperature at the node  $r = 0$  was found by averaging all of the surrounding nodal temperatures. As an initial condition all of the nodes at  $t = 0$  were set to room temperature, 23 degrees Celsius. As a boundary condition the temperature at the outer radius of the water,  $R$ , was maintained at the initial condition temperature. Ultrasound intensity was modeled as a step function beginning at  $t = 0$ .

## Results

Figure 37 shows the heating characteristics of the finite difference model of the insonated clinical thermocouple probe after one second of ultrasound insonation. It can be seen that the quadrant of the probe which "sees" the ultrasound intensity is the portion of the probe that heats due to ultrasound absorption. The heating of the far side of the sheath and heating of the water are due to conduction. It can be seen from the figure that the temperature profile from the insonated side



- A series of new probes were designed, constructed and tested.
- A final design was proposed for future work.

A series of probes have been built focussing on forcing the thermocouples into the center of the probe. These have reduced the variation somewhat and made the variation more reliably sinusoidal, but a transducer has not been built to date that reduces this variation below  $\pm 10\%$ . A new design has been proposed that is intended to further reduce the variation. [29]

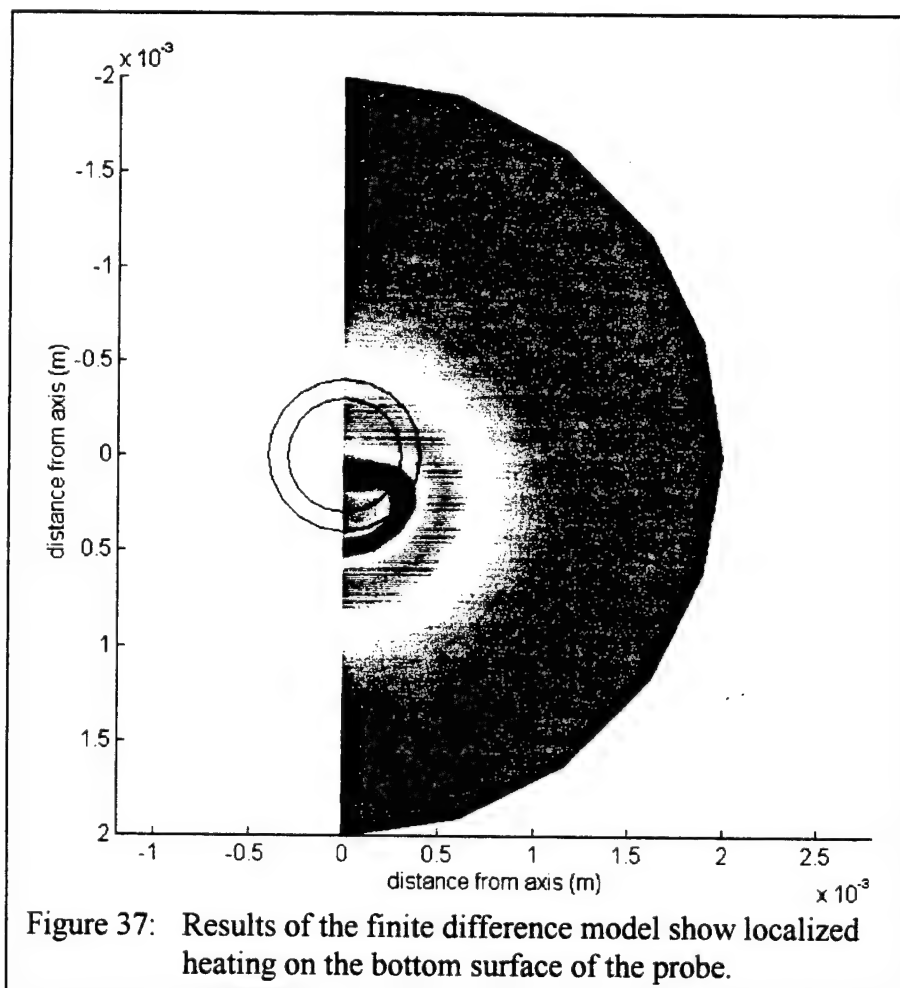
### **Subsystem 3: Model Development**

The model was completed in the 3<sup>rd</sup> year. No work was accomplished on this subsystem during the 4<sup>th</sup> year.

due to ultrasound absorption. The heating of the far side of the sheath and heating of the water are due to conduction. It can be seen from the figure that the temperature profile from the insonated side of the sheath to the far side is decreasing significantly. This supports the postulation that the transient response of a sensor within the clinical thermocouple probe is largely dependent on the position of the sensor within the probe.

According to the finite difference heating pattern of the insonated clinical thermocouple probe it would be expected that if the probe were rotated about its own axis that the effective absorption parameter would be highly dependent on rotation. It would be expected that a plot of the effective absorption parameter magnitude versus the respective rotation for an off centered sensor would be sinusoid-like in nature.

Figure 38 is a plot of the normalized temperature at distances from the probe axis versus theta after one second of insonation. It is clear that the final temperature at a distance from the axis has a sinusoid-like dependence with theta, and increasing the off center distance also increases the magnitude of oscillation. Because the effective absorption parameter is determined by a linear curve fit of temperature rise the variations in temperature rise are directly proportional to the determined effective absorption parameter. Consequently, Figure 38 shows that a probe with a sensor off centered by 0.1-mm will result in  $\pm 22\%$  variation of the effective absorption parameter with probe rotation and a sensor off centered by 0.2-mm will result in approximately  $\pm 43\%$  variation of the effective absorption parameter with probe rotation.



#### **Subsystem 4: Inverse Technique**

##### **Subsystem integration completed.**

- **Technique used successfully to optimize the input power model.**

During the fourth year, the inverse optimization technique discussed in previous reports was integrated with the other subsystems. This provides the anticipated capability to adjust the tissue attenuation values to minimize the error between predicted power deposition values and experimentally measured values. This capability was not implemented however. The ultrasonic attenuation measurement was shown to measure attenuation with an error of  $\pm 10\%$ . These measurements are the input nodal attenuation values for the model (before optimization). Since the experimental SAR measurements were not capable of an error as small as this, the optimization would provide no benefit. The capability for optimization is available when the SAR measurement technique improves sufficiently to provide a benefit.

The optimization routines were used for an alternative application that does provide an increase in accuracy of the model. This involves the optimization of the model prediction for the ultrasound field produced by the treatment transducer. This application is described briefly below (and more completely in [30]):

#### **Optimizing the Power Input Field**

Numerical predictions of the ultrasound field produced by a focused transducer show small but significant variations from the results of experimental measurements when the transducer is modeled as a piston. When the normal velocities on the surface of the modeled transducer are allowed to vary, a more accurate model results. In this work the acoustic field of a 500 kHz spherically focussed transducer was experimentally mapped using a 3 axis motion device and a hydrophone. A model of the transducer was developed using a uniform distribution of point sources on the surface of spherical section. The particle velocities at each point were defined based on control points for a 1-D cubic spline (radial symmetry is assumed). By varying the number and position of control points, different velocity functions for the transducer face can be created (A single control point produces piston-like behavior, two points result in a linear variation, etc.). The control point velocities were optimized using a conjugate gradient minimization algorithm (Polak-Ribiere). A piston model produces results similar to the existing USSPAR model. Using four or more control points reduces the error between model and data by ten percent. The resulting velocity function is reminiscent of a Bessel function, perhaps suggesting that the transducer has a secondary drum-like vibrational mode in addition to the expected piezo-electric mode. Further improvements may be obtained by removing the symmetry constraint using a two-dimensional spline fit.

#### **Introduction**

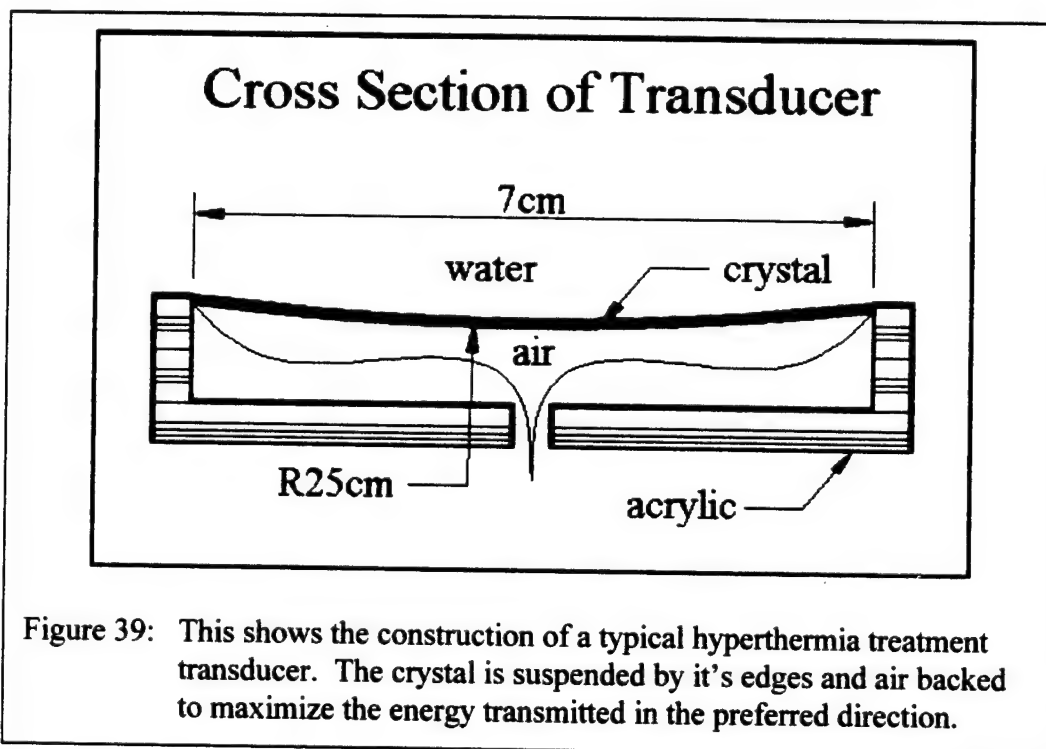
Focused ultrasound transducers are used in hyperthermia cancer treatment therapy. This treatment when combined with radiation has been shown to nearly double the response rates over radiation alone [31]. The goal of the treatment is to uniformly heat a tumor to  $43^{\circ}\text{C}$  [32] while minimizing the temperature rise in the surrounding tissue (Figure 23). To address this problem, numerical models have been created to simulate the hyperthermia temperature field [33-37]. Since such models require an estimate of the power absorbed by the tissue, work is being done to create a more accurate power model. The calibration of the treatment transducer is the first step

in reliably predicting the absorbed power field. One method for doing this is explained by Swindell [38,39]. His model (USSPAR), although it is fast, is based on the assumption that the velocities on the transducer face are constant. More recently, however, models have been developed which allow for variable surface velocities. One uses superimposed Gaussian beams to represent the velocity profile [40], and others break the transducer into elemental areas [41,42].

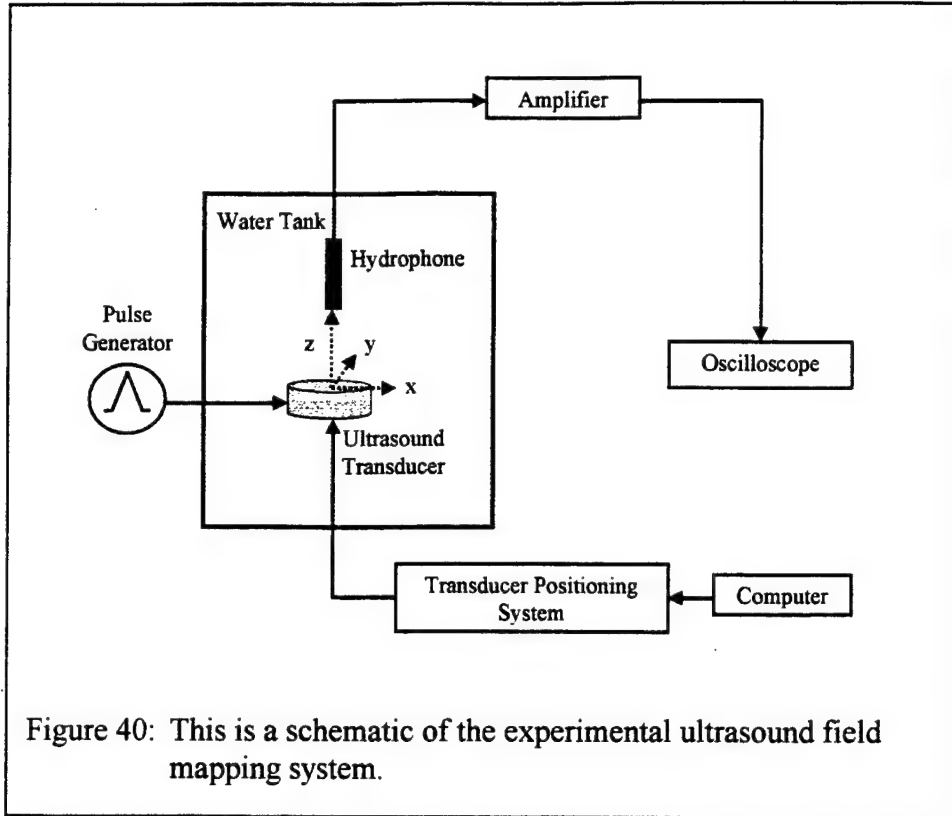
In this work, the transducer is represented as a collection of point sources. The velocities at each point are defined based on control points for a 1-D cubic spline assuming radial symmetry. By varying the number of control points, different velocity functions can be created (A single control point produces piston-like behavior, two points result in a linear variation, etc.). This method was employed to simplify the inverse problem so that large focussed treatment transducers could be calibrated more quickly (Figure 39). A conjugate gradient minimization routine was used to fit the model to data generated by USSPAR as well as measured data.

#### Experimental Setup

Data was measured using a hydrophone and the setup shown in Figure 40. The 500 kHz. transducer shown in Figure 39 was mounted to a 3 axis motion control device which was controlled using a PC. The hydrophone was mounted to a fixed frame inside a tank filled with degassed water. Output from the hydrophone was amplified and read from an oscilloscope. The voltage amplitude was measured and recorded at each data point along with the corresponding scale factor. The intensity was calculated using the experimentally determined calibration factor for the hydrophone at this frequency (500 kHz.):  $I_D = 1.595 \bullet V_{pp}^2$  where  $V_{pp}$  is the peak to peak voltage measured.







## Theory

### The Transducer Model

The transducer was modeled as a group of point sources uniformly distributed on a section of a sphere. This was accomplished by mapping a uniform set of points in a plane onto a sphere. Since the transducer's radius of curvature is much larger than its radius, the error in this approximation is small. The distance between point sources was limited to be about a half a wavelength. The pressure field caused by the transducer was calculated by differentiating the Rayleigh-Sommerfeld diffraction integral producing the following equation:

$$P(r) = \frac{ikZ}{2\pi} \int_S v \frac{e^{-ikr}}{r} ds$$

where  $k = \omega/c = 2\pi/\lambda$  is the wave number,  $\lambda$  is the wavelength,  $Z = \rho c$  is the acoustic impedance of the propagating medium,  $v(r_j) = v_j e^{i\omega t}$  is the normal particle velocity on  $ds$ , and  $r_{ij} = |r_i - r_j|$  is the distance from a point in the field,  $r = r_i$  to a point on the transducer,  $r = r_j$ . If  $ds = (\delta\lambda)^2$  is constant for  $N$  point sources on  $S$  where  $\delta\lambda \ll r$  (not close to transducer) the pressure can be approximated by:  $P_i = iZ\delta^2\lambda \sum_{j=1}^N v_j \frac{e^{-ikr_{ij}}}{r_{ij}}$  where  $\delta \approx \frac{1}{2}$  is the number of wavelengths between points. If  $\tilde{r}_{ij} = r_{ij}/\lambda$ , this simplifies to:

$$P_i = iZ\delta^2 \sum_{j=1}^N v_j \frac{e^{-i2\pi\tilde{r}_{ij}}}{\tilde{r}_{ij}} = iZ\delta^2 \sum_{j=1}^N E_{ij} v_j \text{ where } E_{ij} = \frac{e^{-i2\pi\tilde{r}_{ij}}}{\tilde{r}_{ij}}. \text{ Since } I_i = \frac{\bar{P}_i P_i}{Z} \text{ (no sum on } i), \text{ we get}$$

$$I_i = Z\delta^4 \sum_{k=1}^N \sum_{j=1}^N v_k \bar{E}_{ik} E_{ij} v_j \text{ (}\bar{P}_i \text{ and } \bar{E}_{ik} \text{ are the complex conjugates to } P_i \text{ and } E_{ik} \text{ respectively). To}$$

reduce computation time (by decreasing the dimension of parameter space), and to simultaneously enforce a relatively smooth velocity distribution, a 1-D cubic spline routine is used to interpolate velocities at each point on the transducer (radial symmetry assumption). The velocity profile on the transducer face can then be modified by changing the velocities at the control points. The cubic spline routine generates a transformation matrix which maps model parameters (spline control point velocities) to transducer point velocities. If this matrix ( $T_{jk}$ ) is

$$\text{defined by: } v_j = \sum_{k=1}^M T_{jk} m_k, \text{ the intensity is then: } I_i = Z\delta^4 \sum_{l=1}^M \sum_{k=1}^M m_l \left( \sum_{n=1}^N \sum_{j=1}^N T_{nl} \bar{E}_{in} E_{ij} T_{jk} \right) m_k. \text{ If}$$

tensors are defined such that  $B_{ik} \equiv \sum_{j=1}^N E_{ij} T_{jk}$ , and  $A_{lik} \equiv Z\delta^4 \bar{B}_{il} B_{ik}$  (no sum on  $i$ ), the intensity is

$$\text{then just } I_i = \sum_{l=1}^M \sum_{k=1}^M m_l A_{lik} m_k. \text{ When iterating, only the model parameters (} m \text{) will change so}$$

the third order tensor ( $A_{lik}$ ) needs to be calculated only once and can be easily stored in memory because  $M$  is small.

### Model Optimization Technique

The Conjugate gradient method is used to minimize the error function,  $\Phi \equiv \frac{1}{2} \|I - I_D\|^2$  where  $I_D$  is the measured intensity data. Such methods have been shown to produce favorable results for a wide range of applications [13-16]. The algorithm used here is based on a procedure in *Numerical Recipes in C* [17]. The search direction is defined to be

$$s_{i+1} = -g_{i+1} + \gamma g_i \text{ where } \gamma = \frac{(g_{i+1} - g_i)^T g_{i+1}}{g_i^T g_i} \text{ (Polak-Ribiere). The search starts in the steepest}$$

descent direction ( $g_0 = g_1$ ) and then each subsequent direction is conjugate to all previous ones.

The gradient is found by differentiating with respect to the model parameters,  $m$ :

$$g^T = \frac{\partial \Phi}{\partial m} = (I - I_D)^T J. \text{ The Jacobian is simply } J = \frac{\partial I}{\partial m} = 2mA. \text{ The step length, } \alpha, \text{ for a 1-D}$$

line minimization is found by using a linear approximation for the Intensity

$$(I(m + \alpha s) \approx I(m) + \alpha Js). \text{ The error function becomes } \tilde{\Phi} \equiv \frac{1}{2} \|I - I_D + \alpha Js\|^2. \text{ Minimizing with}$$

$$\text{respect to step length gives } \frac{\partial \tilde{\Phi}}{\partial \alpha} = (I - I_D + \alpha Js)^T Js = 0. \text{ The step length is then } \alpha = \frac{-g^T s}{\|Js\|^2}.$$

## Results

To initially verify the accuracy of the model, theoretical data was generated using USSPAR, an existing power model which calculates the field under the assumption that the velocities on the surface of the transducer are constant [38,39].

The piston velocity profile of both USSPAR and the piston model with one spline point were almost identical. Thus, the piston model fit USSPAR well (misfit,  $Mf = \|I - I_D\| / \|I_D\| \approx 0.0022$ ) but neither did a good job of fitting the data ( $Mf \approx 0.1743$ ). When four spline points were used, however, the fit improved considerably ( $Mf \approx 0.0634$ ). Beyond four points, the misfit didn't decrease much (The 12-point model had  $Mf \approx 0.0620$ ), but the curve became smoother and consequently more believable. As the number of points and point locations changed, the general curve shape remained the same. Finally, reducing the transducer point spacing ( $\delta \approx 0.4$ ) failed to improve the fit ( $Mf \approx 0.0622$ ), indicating that the model points were sufficiently dense to produce an accurate representation of a continuous surface.

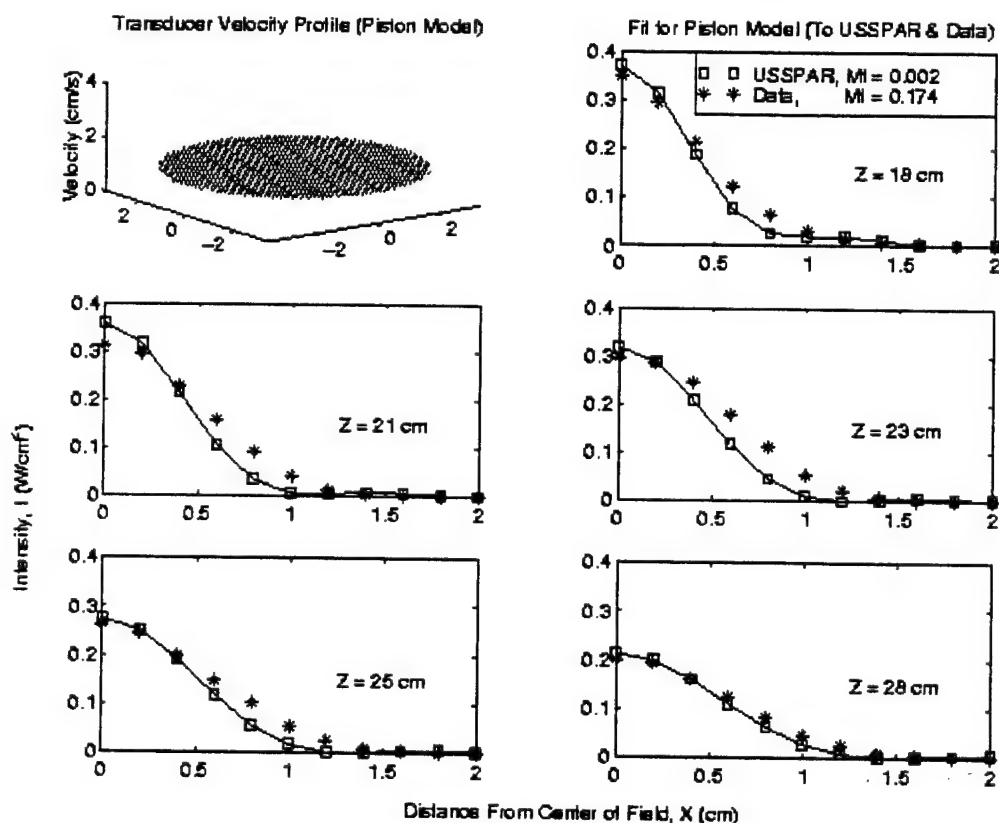


Figure 41: When the model uses a piston-like velocity profile it behaves identically to the USSPAR model, providing a relatively poor match to the experimental data.

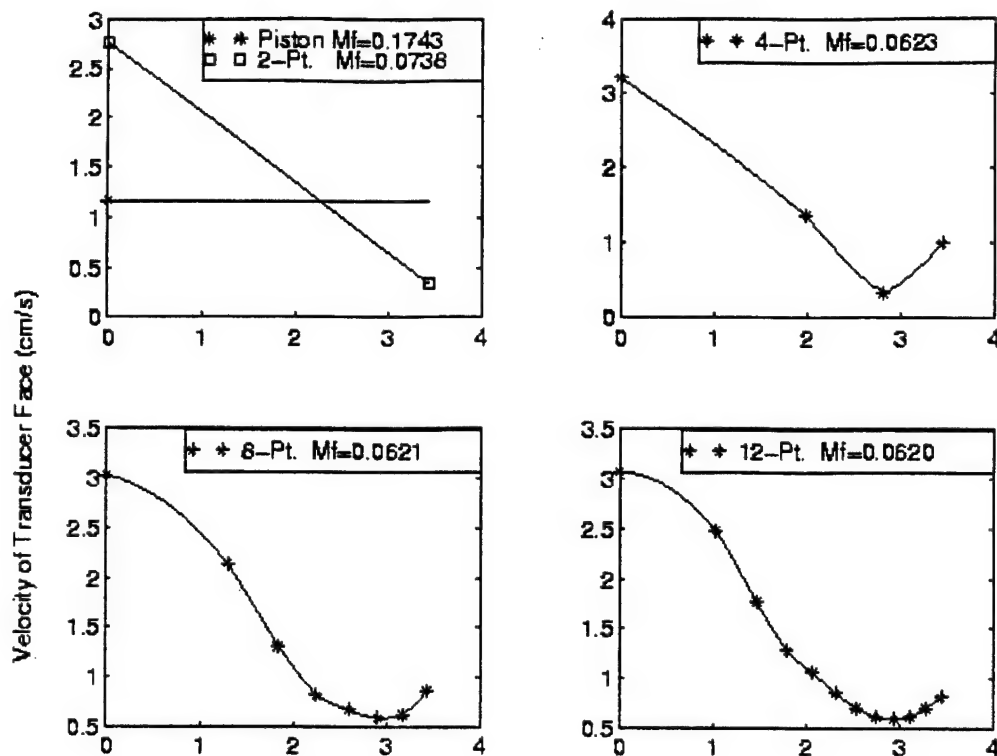


Figure 42: When the surface velocity profile on the transducer face is allowed to vary, the misfit between model data and experimental data is reduced.

## Discussion

The main goal of this research was to develop an accurate model of a focussed transducer, but it was also hoped to obtain a realistic estimate of the transducer's actual surface velocity field. In searching for the actual field, one has the advantage of using physiologic feasibility to help define the solution [48]. Also, when the model uses a realistic velocity profile, it is more likely to predict realistic values outside the range of the data used in the optimization procedure. One of the difficulties in optimization is knowing when to quit. If the data is fit too closely, the model may be fitting experimental noise and consequently give poor results. For these reasons, a smooth solution was one of the goals (It is expected that large variations in velocities would tear the transducer apart). It is also a good sign when varied initial conditions converge to a similar solution. For instance, when more spline points are used, the solution should not change drastically but should be refined. Originally, the resulting curves varied quite dramatically when more points were included. It was then discovered that the convergence tolerance was too small. Once the routine was modified to quit when the misfit began to level out, the solutions all began to look alike regardless of the number of points used.

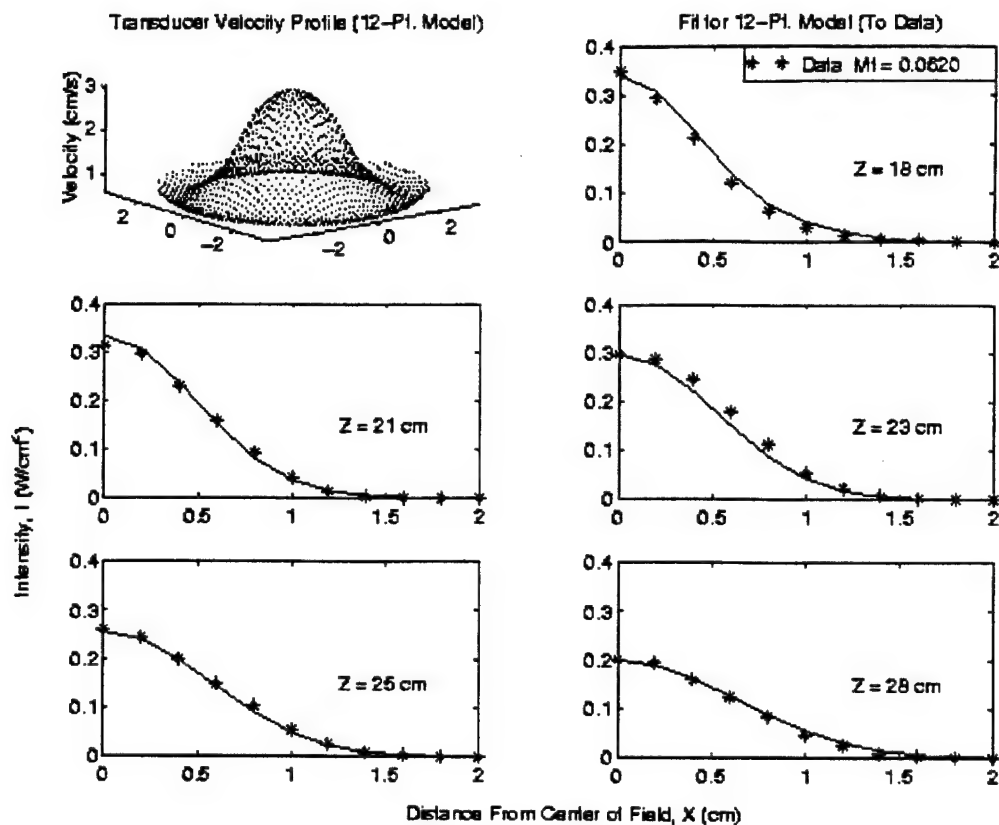


Figure 43: Using 12 spline points provides a significantly improved fit.

The refined velocity function appears to be reminiscent of a Bessel function, which may suggest that the transducer has a secondary drum-like vibrational mode in addition to the expected piezo-electric mode. This may be due somewhat to the construction of the air-backed transducer used (Figure 39). The relatively unconstrained mounting setup should permit some resonant behavior.

When reducing the transducer point spacing failed to improve results, it was decided that the remaining error must lie mainly in the measured data rather than in the model. The model's main assumption is that the transducer can be modeled as a collection of points if they are uniformly spaced and close together. Consequently, increasing the number of points should reduce the error in the model.

## Conclusions and Recommendations

Although it is still uncertain whether the model's surface velocity field agrees with reality, there is reason to believe that it is a good approximation to reality since it is smooth, consistent and fits the data quite well. It has also been shown that allowing the surface velocities to vary can be beneficial. This particular model is not expected to be accurate at close range, however. It is suited particularly for large focussed treatment ultrasound transducers where accuracy in the very near field is not required. This method is quite simple to apply and not computationally expensive. All the code was written using Matlab 5.0 and the 12-point model ( $N=1725$ ,  $D=55$ ) took less than 30 seconds to converge on a Sun SPARC 20 workstation.

Further improvements may be obtained by removing the symmetry constraint using a two-dimensional spline fit. A more detailed discussion of the optimization results can be found in [ ].

- **Given the level of scatter in the experimental SAR measurements, the optimization model was not used to adjust nodal attenuation values.**

## **Conclusions and Recommendations**

The results of this project represent a significant step forward in accuracy for a practical, clinical ultrasound power deposition model for hyperthermia treatment planning. While this is true, accurate power deposition is only one piece of a complete model. This model must be integrated into a complete thermal model. Other issues will continue to limit the accuracy of the thermal models, including unknown perfusion values and changes in the model parameters that result from the treatment. The statement of work included anticipated clinical trials of the system which were not carried out. This is a disappointment and results from the dependence of this work on the clinical data of other researchers. Anticipated clinical tests in the Hyperthermia Lab at the University of Utah Hospital have not yet been conducted.

The system developed here is currently being implemented on the hyperthermia treatment facility at the University of Utah Hospital and clinical trials are anticipated in future work. The implementation of the system developed here in the Hyperthermia Lab involves two steps: First, the hardware must be installed on the clinical system. This was completed as part of the final testing of the system. Second, the model integration mentioned above must be completed. This is currently being investigated by researchers in the Hyperthermia Lab.

As a final recommendation, it is anticipated that the accuracy and value of the model developed here can be improved by further development of an accurate experimental method to measure SAR.

## References

- [1] Anonymous., *JAMA*, 271:797-802, 1994.
- [2] B.A. Bornstein, P.S. Zouranjian, J.L. Hansen, S.M. Fraser, L.A. Gelwan, B.A. Teicher, and G.K. Svensson, *Int. J. Radiation Oncology Biology Physics*, 25:79-85, 1993.
- [3] J. Overgaard, D.G. Gonzalez, M.C.C.M. Hulshof, G. Arcangeli, O. Dahl, O. Mella, and S.M. Bentzen, *Lancet*, 345:540-543, 1995.
- [4] M. Jolley, Masters Thesis, University of Utah, 1996.
- [5] E.J. Halpern, *Investigative Radiology*, 28:598-603, 1993.
- [6] G. Berger, P. Laugier, J.C. Thalabard, and J. Perrin, *Ultrasonic imaging*, 12:47-57, 1990.
- [7] B.W. Dong, M. Wnag, K. Xie, and M.H. Chen, *J. Clinical Ultrasound*, 22:167-174, 1994.
- [8] S.W. Flax, J.P. Norbert, G.H. Glover, F.D. Gutmann, and M. McLachlan, *Ultrasonic Imaging*, 5:95-116, 1983.
- [9] B.S. Garra, M.F. Insana, T.H. Shawker, and M.A. Russell, *Radiology*, 162:61-67, 1987.
- [10] M. Fink, F. Hottier, and J.F. Cardoso, *Ultrasonic Imaging*, 5:117-135, 1983.
- [11] S.A. Goss, R.L. Johnson, F. Dunn, *JASA*, 64:423-457, 1978.
- [12] E. Walach, A. Shmulewitz, Y. Itzhak, and Z. Heyman, *IEEE Transactions on Biomedical Engineering*, 36:211-221, 1989.
- [13] E. Walach, C. N. Liu, R. C. Waag, and K. J. Parker, *IEEE Transactions on Biomedical Engineering*, BME-33:637-643, 1986.
- [14] R. Kuc and M. Schwartz, *IEEE Transactions on Sonics and Ultrasonics*, SU-26:353-362, 1979.
- [15] R. Kuc, *IEEE Transactions on Biomedical Engineering*, BME-27:312-319, 1980.
- [16] I. Cespedes and J. Ophir, *Ultrasound in Medicine and Biology*, 16:707-717, 1990.
- [17] K. J. Parker, M. S. Asztely, R. M. Lerner, E. A. Schenk, and R. C. Waag, *Ultrasound in Medicine and Biology*, 14:127-136, 1988.
- [18] K. Itoh, Y. Yasuda, O. Suzuki, H. Itoh, T. Itoh, T. Jing-Wen, T. Konishi, and A. Koyano, *Journal of Clinical Ultrasound*, 16:553-562, 1988.
- [19] K. Zhou, D. Zhang, C. Lin, and S. Zhu, *JASA*, 92:2532-2538, 1992.
- [20] L. S. Wilson, D. E. Robinson, and B. D. Doust, *Ultrasonic Imaging*, 6:278-292, 1984.
- [21] S. W. Flax, N. J. Pelc, G. H. Glover, F. D. Gutmann, and M. McLachlan, *Ultrasonic Imaging*, 5:95-116, 1983.
- [22] E. J. Halpern, *Investigative Radiology*, 28:598-603, 1993.
- [23] L. S. Wilson, M. L. Neale, H. E. Talhami, and M. Appleberg, *Ultrasound in Medicine and Biology*, 20:529-542, 1994.



- [24] K.J. Parker, *JASA*, 74:1356-1361, 1983.
- [25] M. Lyons and K.J. Parker, *IEEE Trans. Ultrasound Ferroelectrics and Freq. Control*, 35:511-521, 1988.
- [26] R. Kuc, *Proc. IEEE* 73:1159-1168, 1985.
- [27] B. Thurgood, Master's Thesis, Department of Bioengineering, University of Utah, 1998.
- [28] T. Lee, Master's Thesis, Department of Bioengineering, University of Utah, 1998.
- [29] T. Youd, Master's Thesis, Department of Mechanical Engineering, University of Utah, 1998.
- [30] J. Ostler, Master's Thesis, Department of Mechanical Engineering, University of Utah, 1998.
- [31] Sneed, P. K., and Phillips, T. L, *Oncology*, Vol. 5, No. 3, 1991, pp. 99-112.
- [32] Christensen, D. A., *Ultrasonic Bioinstrumentation*, 1988, pp. 167-168.
- [33] Fan, X., and Hynynen, K., *J. Acoust. Soc. Am.* Vol. 91, No. 3, 1992, pp. 1727-1736.
- [34] Fan, X., and Hynynen, K., *Med. Phys.* Vol. 21, No. 1, 1994, pp. 25-34.
- [35] Liauh, C-T., Hills, R. G., and Roemer, R. G., *ASME Journal of Biomechanical Engineering*, Vol. 115, 1993, pp. 63-71.
- [36] Liauh, C-T., Roemer, R. G., *ASME Journal of Biomechanical Engineering*, Vol. 115, 1993, pp. 239-246.
- [37] Liauh, C-T., Roemer, R. G., *ASME Journal of Biomechanical Engineering*, Vol. 115, 1993, pp. 257-261.
- [38] Swindell, W., "Ultrasonic Hyperthermia," *Physical Techniques in Clinical Hyperthermia*, Edited by Hand, J. W., and James, J. R., Research Studies Press LTD. Letenworth, Hartfordshire, England, 1986, pp. 288-326.
- [39] Swindell, W., Roemer, R. B., and Clegg, S. T., *IEEE Ultrasonics Symposium*, 1982, pp. 750-753.
- [40] Zhou, D., and Peirlinckx, L., Lumori, M.L.D., and Van Biesen, L., *J. Acoust. Soc. Am.*, Vol. 99, No. 3, 1996, pp. 1438-1445.
- [41] Fan, X., Moros, E. G., and Straube, W. L., *J. Acoust. Soc. Am.*, Vol. 102, No. 5, 1997, pp. 2734-2741.
- [42] Ocheltree, K. B., and Frizzell, L. A., *IEEE Trans. Ultrason. Ferroelectr. Freq. Control*, Vol. 36, 1989, pp. 242-248.
- 43 Jacobs, D. A. H., *IMA J. Numerical Analysis*, Vol. 6, 1986, pp. 447-452.
- [44] Paige, C. C., and Saunders, M. A., *ACM Trans. on Mathematical Software*, Vol. 8, No. 1, 1982, pp. 43-71.
- [45] Powell, M. J. D., *SIAM Review*, Vol. 28, No. 4, 1986, pp. 487-500.

- [46] Luenberger, D. G., *Linear and Nonlinear Programming (Sec. Ed)*, Addison Wesley, Reading, Mass., 1989.
- [47] Press, W. H., Teukolsky, S. A., Vetterling, W. T., and Flannery, B. P., *Numerical Recipes in C*, 1995, pp. 420-425.
- [48] Johnson, C. R., *IEEE Computational Science & Engineering*, Winter, 1995, pp. 42-48.